PAPER • **OPEN ACCESS**

Effect of dilution gas on the distribution characteristics of capacitively coupled plasma by comparing SiH_4/He and SiH_4/Ar

To cite this article: Ho Jun Kim *et al* 2023 *Plasma Sources Sci. Technol.* **32** 115008

OPEN ACCESS
IOP Publishing
Plasma Sources Science and Technology
Plasma Sources Sci. Technol. **32** (2023) 115008 (21pp)
https://doi.org/10.1088/1361-6595/ad03bc

Effect of dilution gas on the distribution characteristics of capacitively coupled plasma by comparing SiH_4/He and SiH_4/Ar

Ho Jun Kim[1,*], **Kyungjun Lee**[2] **and Hwanyeol Park**[3,4,*]

[1] Department of Mechanical Engineering, Hanyang University ERICA Campus, 55 Hanyangdaehak-ro, Sangnok-gu, Ansan, Gyeonggi-do 15588, Republic of Korea
[2] Department of Mechanical Engineering, Gachon University, 1342 Seongnam-daero, Sujeong-gu, Seongnam-si, Gyeonggi-do 13120, Republic of Korea
[3] Department of Display Materials Engineering, Soonchunhyang University, 22 Soonchunhyang-ro, Sinchang-myeon, Asan-si, Chungcheongnam-do 31538, Republic of Korea
[4] Department of Electronic Materials, Devices, and Equipment Engineering, Soonchunhyang University, Asan City, Chungnam 31538, Republic of Korea

E-mail: hojunkim9158@hanyang.ac.kr, tiger.anima@gmail.com and phy3654@sch.ac.kr

Received 12 June 2023, revised 19 August 2023
Accepted for publication 16 October 2023
Published 7 November 2023

Abstract

In this study, we focus on the difference in the spatial distribution of the plasma parameters between SiH_4/He capacitively coupled plasma (CCP) and SiH_4/Ar CCP. The SiH_4/He mixture is modeled using the chemical reactions that were successfully derived in our previous studies. The chemical reaction model of the SiH_4/Ar mixture built in this study is based on the detailed set of chemical reactions in Ar. The spatial distribution of the plasma parameters is examined with the aid of a 2D fluid model. The electron and radical densities of SiH_4/Ar CCP are higher than those of SiH_4/He CCP. In addition, dilution with Ar results in more uniform reaction rates, which leads to a more uniform deposition profile. Because helium requires higher threshold energies for excitation and ionization, dilution with He had little effect on the precursor production. As a result, the concentration of Si_2H_6 observed in the inter-electrode region when using Ar for dilution was observed to be about ten times higher than the concentration of Si_2H_6 observed for He. This high concentration played a large role in influencing the formation of important radicals that determine the deposition rate as well as the difference in the deposition rate profile between Ar and He as diluents. The higher concentration of Si_2H_6 when using Ar means that the production rate of Si_2H_5 is higher in Ar. An examination of the effect of the dilution gas on the deposition rate profile indicated that the deposition rate profile with Ar is 100% more uniform and the deposition rate nearly 87% higher than for dilution with He.

Keywords: plasma enhanced chemical vapor deposition, capacitively coupled plasma, dilution gas effect, fluid simulation, hydrogenated amorphous silicon

* Authors to whom any correspondence should be addressed.

1. Introduction

Over the past few decades, techniques related to the desired treatment of target surfaces using plasma have been used in a variety of high-tech industrial applications [1–3]. These related technologies typically include plasma enhanced atomic layer deposition, plasma enhanced chemical vapor deposition (PECVD), and dry etching. In the microelectronics industry, the above-mentioned plasma-related technologies are highly important [4]. Our focus, as part of the development of process technology, is on lowering the cost of microchip production and improving the process quality [5, 6]. Representative factors that could be considered to accomplish these goals include the type of dilution gas, gas pressure, power delivery, and utilization of high frequency [7, 8]. The plasma physical/chemical roles of these factors are analyzed to optimize the process conditions.

Capacitively coupled plasma (CCP) is considered to be a highly suitable plasma source for optimization of the process conditions [9–12]. In particular, CCP has been usefully employed for the design of PECVD reactors owing to the wide applicability of this technique. Among the research topics that have been considered important in the field of CCP discharge, the objectives of designing reactors for use as equipment for semiconductor production are to ensure the efficient use of the input power and the rapid and uniform heating of electrons in the discharge volume with the delivered power. Useful approaches to achieving these objectives would be to vary the gas pressure or adjust the excitation frequency. Another simple but effective method would entail changing the dilution gas, whereby it would be possible to control the spatial distribution of the source gas density. In addition, the electron collision reaction rate could be improved, and the uniformity of radio frequency (RF) power deposition could be improved by affecting the average energy dissipation. Furthermore, important discharge characteristics such as the surface flux of ions and radicals measured at the electrode surface could be optimized as a result of changing the dilution gas. Since the control of the plasma density distribution is of great importance to achieve process optimization, the dilution gas in CCP discharges has been studied extensively to determine its effect on the process [13–20].

At the same time, several efforts have been made to elucidate the deposition mechanism of thin films in order to analyze and understand the limitations of the deposition rate. These limitations have been sought to be overcome, for example, by improving the gas-phase reaction. Accordingly, changing the dilution gas is expected to help to increase the deposition rate similar to the way in which the deposition rate of the thin film is improved by changing the RF or gas pressure. In addition, a different dilution gas would enable the properties of the deposited thin films to be improved. Zhang and Zhang found higher-silane related reactive species (HSRS) to be an important factor for increasing the photo-induced degradation of hydrogenated amorphous silicon (a-Si:H) films [20]. They controlled the generation of HSRS with the use of dilution gases such as H_2, He, and Ar.

The deposition of silicon-based thin films using CCP is generally carried out using a larger amount of the dilution gas (Ar, He, or H_2) than the amount of source gas such as SiH_4 and Si_2H_6. In addition, in the thin film formation process, pressure conditions of 100 Pa or more are frequently used to prevent the increase in intrinsic stress caused by ion bombardment and to increase the deposition rate by increasing the efficiency of the generation of radicals in the gas phase reaction. For example, in our previous study of the deposition of an amorphous silicon layer using the SiH_4/He mixture, the amount of SiH_4 used was only 1%–2% of the amount of He used, and the pressure exceeded 400 Pa [8, 21, 22]. Therefore, because of the large proportion of dilution gas in the mixture, the plasma properties of the mixture are inevitably influenced more profoundly by the type of dilution gas.

Based on the aforementioned importance of the dilution gas, in this study, we investigate the difference in the spatial distribution of plasma parameters between SiH_4/He mixture CCP and SiH_4/Ar mixture CCP using a 2D fluid model. In fact, studies on CCP with these two mixtures have been conducted from various perspectives. For example, in our previous research, SiH_4/He mixture CCP was used to determine the conditions under which an amorphous silicon layer could be uniformly and rapidly deposited, and ways in which to establish these conditions were studied [8, 21, 22]. The generation of silicon nanoparticles using SiH_4/Ar CCP was also previously studied [23–27]. However, despite the frequency and importance of using this method, a systematic investigation of the difference between Ar and He as dilution gases does not seem to have been reported yet.

Therefore, in this paper, we present the results of a numerical analysis of the effect of the dilution gas when using SiH_4/He mixture CCP and SiH_4/Ar mixture CCP. Our study revealed various differences in the spatial distribution of the plasma parameters resulting from the thinner plasma sheath thickness when Ar, instead of He, was used as the dilution gas. In addition, the uniformity of the deposition rate profile was found to be consistently good in the case of argon dilution even when the input power was doubled.

2. Method

2.1. Plasma model

A 2D fluid model was used to analyze the spatial distribution of plasma parameters. A self-consistent model was adopted to accurately analyze the plasma density distribution according to changes in the dilution gas and process conditions. The model considered the following physical factors: RF plasma discharges, convection resulting from gas flow, thermal energy balance by chemical reactions, balance of thermal energy according to the difference in gas temperature caused by boundary conditions, distribution of source gas density, and gas-phase reactions and surface reactions caused by the RF plasma. As the details were elaborated in our previous articles

[8, 21, 22], only the corresponding governing equations are briefly introduced here as follows:

$$\frac{\partial \rho}{\partial t} = -\nabla \cdot (\rho \mathbf{v}), \tag{1}$$

$$\frac{\partial}{\partial t}(\rho \mathbf{v}) = -\nabla \cdot (\rho \mathbf{v}\mathbf{v}) - \nabla p_{\mathrm{g}} - \nabla \cdot (\boldsymbol{\tau}) + \mathbf{f}, \tag{2}$$

$$\boldsymbol{\tau} = -\mu \left[\left(\nabla \mathbf{v} + (\nabla \mathbf{v})^{T} \right) - \frac{2}{3} (\nabla \cdot \mathbf{v}) \mathbf{I} \right], \tag{3}$$

$$\frac{\partial}{\partial t}(\rho Y_i) = -\nabla \cdot (\rho \mathbf{v} Y_i) - \nabla \cdot \left(j_i^{\mathrm{C}} + j_i^{\mathrm{T}} \right) + (G_i - L_i) M_i, \tag{4}$$

$$\frac{\partial n_{\mathrm{e}}}{\partial t} + \nabla \cdot J_{\mathrm{e}} = S_{\mathrm{e}}, \tag{5}$$

$$J_{\mathrm{e}} = -D_{\mathrm{e}} \nabla n_{\mathrm{e}} + \mu_{\mathrm{e}} n_{\mathrm{e}} \nabla \phi, \tag{6}$$

$$\frac{\partial (n_{\mathrm{e}} \varepsilon)}{\partial t} + \nabla \cdot \left[\frac{5}{3} n_{\mathrm{e}} \varepsilon \mathbf{v}_{\mathrm{e}} - \frac{5}{3} n_{\mathrm{e}} D_{\mathrm{e}} \nabla \varepsilon \right] = -e J_{\mathrm{e}} \cdot E - n_{\mathrm{e}} N k_{\mathrm{l}}(\varepsilon), \tag{7}$$

$$\nabla^2 \phi = -\frac{e}{\varepsilon_0} (n_{\mathrm{p}} - n_{\mathrm{e}} - n_q), \tag{8}$$

where ρ is the overall density, t is the time, $\mathbf{v}$ is the overall velocity, p_{g} is the gas pressure, $\boldsymbol{\tau}$ is the viscous stress tensor, $\mathbf{f}$ is the net force per unit volume, μ is the molecular viscosity, Y_i is the mass fraction of species i, j_i^{C} is the flux of species i resulting from the concentration gradients, j_i^{T} is the thermal diffusion flux of species i, G_i is the rate at which species i is generated, and L_i is the rate at which species i is depleted, M_i is the molar mass of species i, n_{e} is the electron density, J_{e} is the electron flux, S_{e} is the electron source, D_{e}, is the electron diffusion coefficient, μ_{e}, is the electron mobility, ϕ is the electric potential, ε is the electron energy, $\mathbf{v}_{\mathrm{e}}$ is the electron velocity, $-e$ is the electron charge, E is the electric field, N is the neutral density, k_{l} is the electron energy loss, ε_0 is the permittivity of space, n_{p} is the positive ion density, and n_q is the negative ion density. In equation (3), $\mathbf{I}$ is the unit matrix. In the case of Ar dilution, the gas velocity is decreased.

To reduce the calculation time, the 0D Boltzmann equation was solved before simulation of the 2D CCP. This solution enabled the electron energy distribution function to be obtained, whereupon the parameters related to the electron impact reaction rate and electron transport were obtained. A lookup table was created as a result of the calculations performed in this preprocessing step.

2.2. Plasma chemistry

In this study, we considered various neutral and charged species that can be observed in SiH_4/He and SiH_4/Ar discharges. These species include radical species, positive and negative ions, and stable and excited molecules produced from SiH_4, He, and Ar. In addition, a sticking model was used to numerically analyze the thin film deposition phenomenon. The probability coefficients of various reactive radicals, obtained from the experimental results of other researchers, were used in this sticking model [28–30].

The probability coefficient of silicon ions was assumed to be a unit probability value. Additionally, first-principle density functional theory calculations were conducted on hydrogenated (H-covered) Si(001) and Si(111) surfaces to investigate Si_2H_6 surface reactivity [31, 32].

The chemical reaction model of the SiH_4/He mixture is the model we successfully used in our previous research [8, 21, 22]. The chemical reaction model of the SiH_4/Ar mixture was constructed by building a detailed set of chemical reactions for this mixture and this model was applied in this study to achieve completeness of the results. Because Ar was used as the dilution gas, the chemistry of Ar was considered in detail and was verified via a quantitative comparison with the measurement results acquired with the Langmuir probe in our previous study [33].

With regard to the chemical processes involving SiH_4/Ar mixtures, we used a subset of the reactions discussed in previous reports [21, 22, 28]. A total of more than 200 gas-phase chemical reaction equations were considered in the SiH_4/Ar chemical reaction model to ensure the completeness of the numerical analysis results. The electron impact reactions included ionization, dissociation, and dissociative attachment. SiH_4/Ar discharges were considered to contain 14 charged species, namely Si^+, SiH^+, SiH_2^+, SiH_3^+, H^+, H_2^+, H_3^+, $Si_2H_2^+$, $Si_2H_4^+$, Ar^+, Ar_2^+, SiH_3^-, SiH_2^-, and e^- (an electron). We also considered 25 neutral species, namely SiH_4, $SiH_4^{(1-3)}$, $SiH_4^{(2-4)}$, Si, SiH, SiH_2, SiH_3, Si_2H_2, Si_2H_4, Si_2H_5, Si_2H_6, Si_3H_7, Si_3H_8, Si_4H_9, Si_4H_{10}, Si_5H_{11}, Si_5H_{12}, H_2, $H_2^{(v=1)}$, $H_2^{(v=2)}$, $H_2^{(v=3)}$, H, Ar, $Ar(^3P_2)$, $Ar(^3P_1)$, $Ar(^3P_0)$, $Ar(^1P_1)$, Ar(4p), and $Ar_2{}^*$. In table 1, we list selected gas-phase reactions considered to play an important role in the formation of radicals under the condition that the gas pressure exceeds 100 Pa. For brevity of notation, table A1 in the appendix lists the remaining gas phase reactions.

Furthermore, comparison of the deposition rate profiles of the amorphous silicon layers deposited using CCP simulations with the experimental values confirmed the validity of the reaction model. This comparison is presented section 3.

2.3. Surface model

A sticking model was used to numerically analyze the thin film deposition phenomenon. The probability coefficients of various reactive radicals, obtained from the experimental results of other researchers, were used in this sticking model [22].

The deposition can be described by a sticking model, which is obtained as follows:

$$-D_i \frac{\partial n_i}{\partial z} = -R_{i,s}(n_{i,s}) = \Gamma_i^{\mathrm{in}} + \Gamma_i^{\mathrm{out}}, \tag{9}$$

where subscript i is the species index, D_i is the diffusion coefficient, n_i is the density of species i, z is the axial coordinate, $n_{i,s}$ is the density of species i at the surface, and $R_{i,s}$ is the surface reaction rate of species i, respectively. In equation (9), the flux of species i, which reacts at the surface, is obtained as follows:

$$\Gamma_i^{\mathrm{in}} = \frac{s_i + \gamma_i}{1 - (s_i + \gamma_i)/2} n_{i,s} \sqrt{\frac{k_{\mathrm{B}} T_{\mathrm{g}}}{2\pi M_i}}, \tag{10}$$

Table 1. Selected gas-phase reactions considered in this study.

No	Reactions	Reaction rate coefficients	References
	Homogeneous pyrolysis		
R01	$SiH_4 \leftrightarrow SiH_2 + H_2$	Pre-exponential factor: $A_k = 1.09 \times 10^{25}$ (mol, m^3, s) Temperature exponent: $\beta_k = -3.37$ (−) Activation energy: $E_k = 256$ (kJ mol^{-1})	[22, 28, 34]
R02	$SiH_4 \leftrightarrow SiH_3 + H$	Pre-exponential factor: $A_k = 3.69 \times 10^{15}$ (mol, m^3, s) Temperature exponent: $\beta_k = 0.0$ (−) Activation energy: $E_k = 390$ (kJ mol^{-1})	[22, 28, 34]
R03	$Si_2H_6 \leftrightarrow SiH_4 + SiH_2$	Pre-exponential factor: $A_k = 3.24 \times 10^{29}$ (mol, m^3, s) Temperature exponent: $\beta_k = -4.24$ (−) Activation energy: $E_k = 243$ (kJ mol^{-1})	[22, 28, 34]
	Ar-SiH_x reactions		
R04	$Ar^* + H_2 \rightarrow Ar + H + H$	7.00×10^{-17} (m^{3}s^{-1})	[28, 35]
R05	$Ar^* + SiH_4 \rightarrow Ar + SiH_3 + H$	1.40×10^{-16} (m^{3}s^{-1})	[28, 35]
R06	$Ar^* + SiH_4 \rightarrow Ar + SiH_2 + H + H$	2.60×10^{-16} (m^{3}s^{-1})	[28, 35]
R07	$Ar^* + SiH_3 \rightarrow Ar + SiH_2 + H$	1.00×10^{-16} (m^{3}s^{-1})	[28, 35]
R08	$Ar^* + SiH_2 \rightarrow Ar + SiH + H$	1.00×10^{-16} (m^{3}s^{-1})	[28, 35]
R09	$Ar^* + SiH \rightarrow Ar + Si + H$	1.00×10^{-16} (m^{3}s^{-1})	[28, 35]
R10	$Ar^* + Si_2H_6 \rightarrow Ar + Si_2H_4 + H + H$	6.60×10^{-16} (m^{3}s^{-1})	[28, 35]
R11	$Ar^* + Si_2H_4 \rightarrow Ar + Si_2H_2 + H + H$	6.60×10^{-16} (m^{3}s^{-1})	[28, 35]
R12	$Ar^{**} + H_2 \rightarrow Ar + H + H$	7.00×10^{-17} (m^{3}s^{-1})	[28, 35]
R13	$Ar^{**} + SiH_4 \rightarrow Ar + SiH_3 + H$	1.40×10^{-16} (m^{3}s^{-1})	[28, 35]
R14	$Ar^{**} + SiH_4 \rightarrow Ar + SiH_2 + H + H$	2.60×10^{-16} (m^{3}s^{-1})	[28, 35]
R15	$Ar^{**} + SiH_3 \rightarrow Ar + SiH_2 + H$	1.00×10^{-16} (m^{3}s^{-1})	[28, 35]
R16	$Ar^{**} + SiH_2 \rightarrow Ar + SiH + H$	1.00×10^{-16} (m^{3}s^{-1})	[28, 35]
R17	$Ar^{**} + SiH \rightarrow Ar + Si + H$	1.00×10^{-16} (m^{3}s^{-1})	[28, 35]
R18	$Ar^{**} + Si_2H_6 \rightarrow Ar + Si_2H_4 + H + H$	6.60×10^{-16} (m^{3}s^{-1})	[28, 35]
R19	$Ar^{**} + Si_2H_4 \rightarrow Ar + Si_2H_2 + H + H$	6.60×10^{-16} (m^{3}s^{-1})	[28, 35]
	SiH_x reactions		
R20	$H_2{}^+ + H_2 \rightarrow H_3^+ + H$	2.10×10^{-15} (m^{3}s^{-1})	[21, 28, 36]
R21	$SiH_4 + H_3{}^+ \rightarrow SiH_3^+ + H_2 + H_2$	5.16×10^{-16} (m^{3}s^{-1})	[21, 28, 37]
R22	$SiH_4 + H_2{}^+ \rightarrow SiH_2^+ + H_2 + H_2$	6.59×10^{-17} (m^{3}s^{-1})	[21, 28, 37]
R23	$SiH_4 + H_2{}^+ \rightarrow SiH_3^+ + H_2 + H$	6.23×10^{-16} (m^{3}s^{-1})	[21, 28, 37]
R24	$SiH_4 + H^+ \rightarrow SiH_3^+ + H_2$	5.00×10^{-16} (m^{3}s^{-1})	[21, 28]
R25	$SiH_3{}^+ + SiH_4 \rightarrow Si_2H_2{}^+ + H_2 + H_2 + H$	2.50×10^{-17} (m^{3}s^{-1})	[21, 28]
R26	$SiH_3{}^- + SiH_2{}^+ \rightarrow SiH_3 + SiH_2$	2.50×10^{-13} (m^{3}s^{-1})	[21, 28]
R27	$SiH_3{}^- + SiH_3{}^+ \rightarrow SiH_3 + SiH_3$	5.00×10^{-13} (m^{3}s^{-1})	[21, 28]
R28	$SiH_3{}^- + Si_2H_4{}^+ \rightarrow SiH_3 + SiH_2 + SiH_2$	1.00×10^{-13} (m^{3}s^{-1})	[21, 28]
R29	$SiH_3{}^- + H_2{}^+ \rightarrow SiH_3 + H_2$	1.00×10^{-13} (m^{3}s^{-1})	[21, 28]
R30	$SiH_2{}^+ + SiH_4 \rightarrow Si_2H_4{}^+ + H_2$	2.50×10^{-16} (m^{3}s^{-1})	[21, 28, 38]
R31	$SiH_2{}^+ + SiH_4 \rightarrow SiH_3^+ + SiH_3$	1.07×10^{-15} (m^{3}s^{-1})	[21, 28, 39]
R32	$SiH_2{}^+ + H_2 \rightarrow SiH_3^+ + H$	1.01×10^{-16} (m^{3}s^{-1})	[21, 28, 37]
R33	$SiH_2{}^+ + SiH_4 \rightarrow Si_2H_2{}^+ + H_2 + H_2$	5.50×10^{-17} (m^{3}s^{-1})	[21, 28, 39]
R34	$SiH_2{}^+ + SiH_4 \rightarrow Si_2H_2{}^+ + H_2 + H + H$	7.00×10^{-17} (m^{3}s^{-1})	[21, 28, 40]
R35	$SiH_2{}^+ + Si_2H_6 \rightarrow Si_2H_2{}^+ + SiH_4 + H_2$	3.10×10^{-16} (m^{3}s^{-1})	[21, 28, 41]
R36	$SiH^+ + SiH_4 \rightarrow SiH_3^+ + SiH_2$	6.00×10^{-17} (m^{3}s^{-1})	[21, 28, 39]
R37	$SiH^+ + SiH_4 \rightarrow SiH_2^+ + SiH_3$	1.95×10^{-16} (m^{3}s^{-1})	[21, 28, 39]

(Continued.)

Table 1. (Continued.)

R38	$SiH^+ + SiH_4 \rightarrow Si_2H_2{}^+ + H_2 + H$	5.20×10^{-17} (m^3s^{-1})	[21, 28, 39]
R39	$Si^+ + SiH_4 \rightarrow Si_2H_2{}^+ + H_2$	4.80×10^{-16} (m^3s^{-1})	[21, 28, 39]
R40	$Si^+ + Si_2H_6 \rightarrow Si_2H_2{}^+ + SiH_4$	7.80×10^{-16} (m^3s^{-1})	[21, 28, 41]
R41	$SiH_4 + H \rightarrow H_2 + SiH_3$	2.80×10^{-17} $\exp(-1250/T_g(K))$ (m^3s^{-1})	[21, 28, 42]
R42	$SiH_4 + SiH_3 \rightarrow Si_2H_5 + H_2$	1.78×10^{-21} (m^3s^{-1})	[21, 28, 34]
R43	$SiH_4 + SiH_2 \rightarrow Si_2H_6$	2.00×10^{-16} $[1-(1+0.0032p(Pa))^{-1}]$ (m^3s^{-1})	[21, 28, 43]
R44	$SiH_4 + SiH \rightarrow Si_2H_5$	2.50×10^{-18} (m^3s^{-1})	[21, 28, 44]
R45	$SiH_4 + Si \rightarrow SiH_2 + SiH_2$	5.33×10^{-19} (m^3s^{-1})	[21, 28, 34]
R46	$SiH_4 + Si_2H_4 \rightarrow Si_3H_8$	1.00×10^{-17} (m^3s^{-1})	[21, 28]
R47	$SiH_4 + Si_2H_5 \rightarrow Si_2H_6 + SiH_3$	5.00×10^{-19} (m^3s^{-1})	[21, 28]
R48	$SiH_3 + SiH_3 \rightarrow SiH_2 + SiH_4$	1.50×10^{-16} (m^3s^{-1})	[21, 28, 45]
R49	$SiH_3 + H \rightarrow SiH_2 + H_2$	1.00×10^{-16} (m^3s^{-1})	[21, 28]
R50	$SiH_3 + SiH_2 \rightarrow Si_2H_5$	3.77×10^{-19} (m^3s^{-1})	[21, 28, 44]
R51	$SiH_3 + Si_2H_5 \rightarrow Si_3H_8$	1.00×10^{-17} (m^3s^{-1})	[21, 28]
R52	$SiH_2 + H_2 \rightarrow SiH_4$	3.00×10^{-18} $[1-(1+2.3\times10^{-4}p(Pa))^{-1}]$ (m^3s^{-1})	[21, 28, 43]
R53	$SiH_2 + H \rightarrow SiH + H_2$	7.96×10^{-19} (m^3s^{-1})	[21, 28, 44]
R54	$SiH_2 + H \rightarrow SiH_3$	1.11×10^{-18} (m^3s^{-1})	[21, 28, 44]
R55	$SiH_2 + Si \rightarrow Si_2H_2$	4.53×10^{-19} (m^3s^{-1})	[21, 28, 34]
R56	$SiH_2 + Si_2H_6 \rightarrow Si_3H_8$	4.20×10^{-16} $[1-(1+0.0033p(Pa))^{-1}]$ (m^3s^{-1})	[21, 28, 43]
R57	$SiH_2 + Si_3H_8 \rightarrow Si_4H_{10}$	4.20×10^{-16} $[1-(1+0.0033p(Pa))^{-1}]$ (m^3s^{-1})	[21, 28, 43]
R58	$SiH_2 + Si_4H_{10} \rightarrow Si_5H_{12}$	4.20×10^{-16} $[1-(1+0.0033p(Pa))^{-1}]$ (m^3s^{-1})	[21, 28, 43]
R59	$SiH + Si_2H_6 \rightarrow Si_3H_7$	1.00×10^{-17} (m^3s^{-1})	[21, 28]
R60	$SiH + H_2 \rightarrow SiH_3$	1.98×10^{-18} (m^3s^{-1})	[21, 28, 34]
R61	$Si + H_2 \rightarrow SiH_2$	6.59×10^{-18} (m^3s^{-1})	[21, 28, 34]
R62	$Si_2H_2 + H_2 \rightarrow Si_2H_4$	1.40×10^{-17} (m^3s^{-1})	[21, 28, 34]
R63	$Si_2H_4 + H_2 \rightarrow SiH_4 + SiH_2$	3.56×10^{-15} (m^3s^{-1})	[21, 28, 34]
R64	$Si_2H_4 + H_2 \rightarrow Si_2H_6$	5.33×10^{-19} (m^3s^{-1})	[21, 28, 34]
R65	$Si_2H_5 + Si_2H_5 \rightarrow Si_4H_{10}$	1.50×10^{-16} (m^3s^{-1})	[21, 28]
R66	$Si_3H_7 + H \rightarrow Si_3H_8$	1.00×10^{-17} (m^3s^{-1})	[21, 28]
R67	$Si_4H_9 + H \rightarrow Si_4H_{10}$	1.00×10^{-17} (m^3s^{-1})	[21, 28]
R68	$Si_5H_{11} + H \rightarrow Si_5H_{12}$	1.00×10^{-17} (m^3s^{-1})	[21, 28]
R69	$Si_2H_6 + H \rightarrow Si_2H_5 + H_2$	1.60×10^{-16} $\exp(-1250/T_g(K))$ (m^3s^{-1})	[21, 28, 42]
R70	$Si_2H_6 + H \rightarrow SiH_3 + SiH_4$	8.00×10^{-17} $\exp(-1250/T_g(K))$ (m^3s^{-1})	[21, 28, 42]
R71	$Si_3H_8 + H \rightarrow Si_3H_7 + H_2$	2.40×10^{-16} $\exp(-1250/T_g(K))$ (m^3s^{-1})	[21, 28, 42]
R72	$Si_4H_{10} + H \rightarrow Si_4H_9 + H_2$	2.40×10^{-16} $\exp(-1250/T_g(K))$ (m^3s^{-1})	[21, 28, 42]
R73	$Si_5H_{12} + H \rightarrow Si_5H_{11} + H_2$	2.40×10^{-16} $\exp(-1250/T_g(K))$ (m^3s^{-1})	[21, 28, 42]
R74	$SiH_4{}^{(2-4)} + SiH_4 \rightarrow SiH_4 + SiH_4$	1.92×10^{-19} (m^3s^{-1})	[21, 28, 46]
R75	$SiH_4{}^{(2-4)} + H_2 \rightarrow H_2 + SiH_4$	3.05×10^{-18} (m^3s^{-1})	[21, 28, 46]
R76	$SiH_4{}^{(2-4)} + Si_2H_6 \rightarrow Si_2H_6 + SiH_4$	5.71×10^{-17} (m^3s^{-1})	[21, 28, 46]
R77	$SiH_4{}^{(1-3)} + SiH_4 \rightarrow SiH_4 + SiH_4{}^{(2-4)}$	6.08×10^{-17} (m^3s^{-1})	[21, 28, 46]
R78	$SiH_4{}^{(1-3)} + H_2 \rightarrow H_2 + SiH_4{}^{(2-4)}$	1.53×10^{-16} (m^3s^{-1})	[21, 28, 46]
R79	$SiH_4{}^{(1-3)} + Si_2H_6 \rightarrow Si_2H_6 + SiH_4{}^{(2-4)}$	3.00×10^{-16} (m^3s^{-1})	[21, 28, 46]
	Ion–ion neutralization		
R80	$SiH_n{}^- + Si_lH_m{}^+ \rightarrow SiH_n + Si_lH_m$	5.00×10^{-13} (m^3s^{-1})	[21, 28]
R81	$SiH_n{}^- + M^+ \rightarrow M + SiH_n$	1.00×10^{-13} (m^3s^{-1})	[21, 28]

where subscript *i, s, γ, k_B, T_g*, and M_i are the species index, the sticking coefficient, the recombination probability, the Boltzmann constant, the gas temperature, and the mass of species *i*, respectively. Note that the loss probability β is defined as $\beta = s + \gamma$. The flux to be reflected back into the discharge volume is obtained as follows:

$$\Gamma_i^{\text{out}} = -\sum_{j \neq i} \frac{\gamma_j}{s_j + \gamma_j} \Gamma_j^{\text{in}} \tag{11}$$

where subscript *j* is the species index.

Finally, the deposition rate can be calculated by using the equations below:

$$\Phi_i = \frac{\alpha_i \left(\frac{s_i+\gamma_i}{1-(s_i+\gamma_i)/2} n_{i,s} \sqrt{\frac{k_B T_g}{2\pi M_i}} \right)}{n_s} \left(\frac{s_i}{\beta_i} \right), \tag{12}$$

$$n_s = \frac{N_A \rho}{M}, \tag{13}$$

where Φ_i, α_i, n_s, N_A, M, and ρ are the deposition rate of species *i*, the stoichiometry of species *i*, the surface density of the film,

the Avogadro number, the molar mass of the film, and the mass density of the film, respectively.

2.4. Experimental setup

The shape and operation method of the CCP reactor used in our experiment are the same as those of the CCP reactor considered in the simulation. Therefore, the reaction volume of the reactor during the experiment was used as the simulation domain. Details of the simulation domain will be provided at a later stage.

To verify the simulation results, the experiment was conducted by applying the same process conditions considered in the simulation. The deposition rate profile predicted in the simulation was compared with the experimentally measured deposition rate profile. In order to predict the deposition rate profile from the simulation results, the physical properties of the a-Si:H layer were measured. These physical properties were measured using an x-ray diffractometer (SmartLab, Rigaku Corporation, Japan) and an ellipsometer (SFX-200, KLA Tencor, USA) [47]. The thickness of the a-Si:H layer was measured using the ellipsometer, and the value obtained by dividing the measured thickness by the total deposition time is the deposition rate. These measurements confirmed that the spatial distribution of the refractive index value of the a-Si:H layer deposited on the Si wafer using our CCP reactor was highly uniform (spatial non-uniformity $< 1\%$). Measurement of the film density ($\rho_{\mathrm{Si}} = 2.3$ g cm^{-3}) indicated that the spatial unevenness of this density was less than 1%, and a highly uniform distribution was observed. Based on the distribution of these physical properties, it was confirmed that the film had constant properties in the radial direction. As these uniform film properties were secured, the deposition model based on the radical surface flux was able to derive results that were in good agreement with the experimental results.

3. Results

The showerhead CCP deposition reactor, including its geometric configuration and operating conditions, are described next. Figure 1 shows a schematic representation of the reactor we are considering. Owing to its symmetric nature, the reactor can be represented with only half of its radial and axial coordinates in the *r*-*z* plane. A cylindrical reactor is normally used to process wafers. The borders on the left and right side of the diagram show the symmetrical axis and a sidewall, respectively. Our cylindrical CCP reactor has a top electrode (showerhead electrode), which is separated from the ring-shaped dielectric component. A SiH_4/Ar or SiH_4/He gas mixture is supplied uniformly in the radial direction through the showerhead electrode. In 2D CCP simulations and experimental measurements, this showerhead electrode is powered by RF at 13.56 MHz. The lower electrode (heater) is heated and grounded. Ring-shaped components have an inner surface that acts as a sidewall. In table 2, we summarize the detailed process conditions for each of the cases considered in this study.

As discussed in the introduction, the goal of this study is to clarify the effect of the dilution gas. To this end, the concentration of SiH_4 was set very low at 2%. To establish a baseline, we first analyzed the spatial distribution of the plasma parameters in our reactor using only argon. As mentioned above, the Ar chemistry in the torr regime was verified by comparing the results with the experimental values measured in our previous study. The spatial distributions of the excitation ($Ar + e^- \rightarrow Ar^* + e^-$) rates (kmol m^{-3} s^{-1}), ionization ($Ar + e^- \rightarrow Ar^+ + e^- + e^-$) rates (kmol m^{-3} s^{-1}), Ar^* densities (m^{-3}), and Ar^+ densities (m^{-3}) for Case 1 are displayed in figures 2(a)–(d), respectively. The gas pressure, applied RF power, and Ar flow rate were set at 400 Pa, 200 W, and 5000 sccm, respectively.

The electron collision reaction rates shift towards the bottom grounded electrode as the plasma sheath heats the electrons (figures 2(a) and (b)). The source functions for Ar^* and Ar^+ have the similar shape: the enhanced electrical fields at the electrode edge result in radial extremes in the excitation and ionization rates. This increases the sheath heating, which also results in a shift towards the bottom grounded electrode. Figure 2(c) shows that the Ar^* density in the bulk region varies only slightly. In the corners, converging sheaths produce a high heating rate, resulting in high Ar^* density. The electrons diffuse axially from the production site, with a maximum Ar^+ density seen near the maximum distribution of the ionization rate, as shown in figure 2(d).

3.1. Effects of dilution gas on spatial distributions of plasma parameters

The focus of this section is our observation that a change in dilution gas affects the spatial variation of the plasma parameters such as the distributions of excited species of the dilution gas (i.e. He^* is produced in the case of SiH_4/He and Ar^* is produced in the case of SiH_4/Ar), distributions of ionic species of the dilution gas (the production of He^+ and Ar^+ in the case of SiH_4/He and SiH_4/Ar, respectively), and distributions of electron densities (N_e) and ion fluxes.

We display the excitation rate distributions of the dilution gases in figure 3(a) for the case of SiH_4/He (Case 2; $e^- + He \rightarrow He^* + e^-$) and in figure 3(b) for the case of SiH_4/Ar (Case 3; $e^- + Ar \rightarrow Ar^* + e^-$). The distributions of excited species of the dilution gases are shown in figure 3(c) for the case of SiH_4/He (Case 2; He^*) and in figure 3(d) for the case of SiH_4/Ar (Case 3; Ar^*) to observe the effects of the dilution gas thereon. The following input conditions common to both dilution gases were set: the RF power was set at 200 W, the SiH_4 gas flow was set at 100 sccm, and the gas pressure was set at 400 Pa. The flow rates of both dilution gases were also set as 5000 sccm (table 2): the He gas flow rate was set at 5000 sccm in Case 2, and the Ar gas flow rate was set at 5000 sccm in Case 3.

As shown in figures 3(a) and (b), a shift in the axial direction is observed towards the bottom grounded electrode near the electrode edge, which increases the excitation rate as electrons are heated by the plasma sheath. As depicted in figure 1,

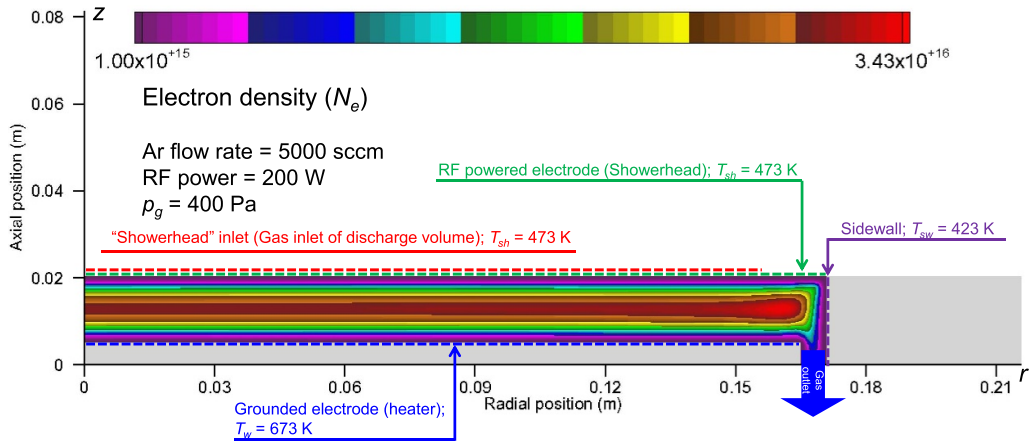

Figure 1. Schematic representation of the CCP reactor we are considering. Spatial variation in the electron density (m^{-3}) for Case 1 (as specified in table 2).

Table 2. List of cases considered in this study.

Case no.	Dilution gas flow rate	SiH_4 flow rate	RF power
1	Ar 5000 sccm	—	200 W
2	He 5000 sccm	100 sccm	200 W
3	Ar 5000 sccm	100 sccm	200 W
4	He 5000 sccm	100 sccm	400 W
5	Ar 5000 sccm	100 sccm	400 W

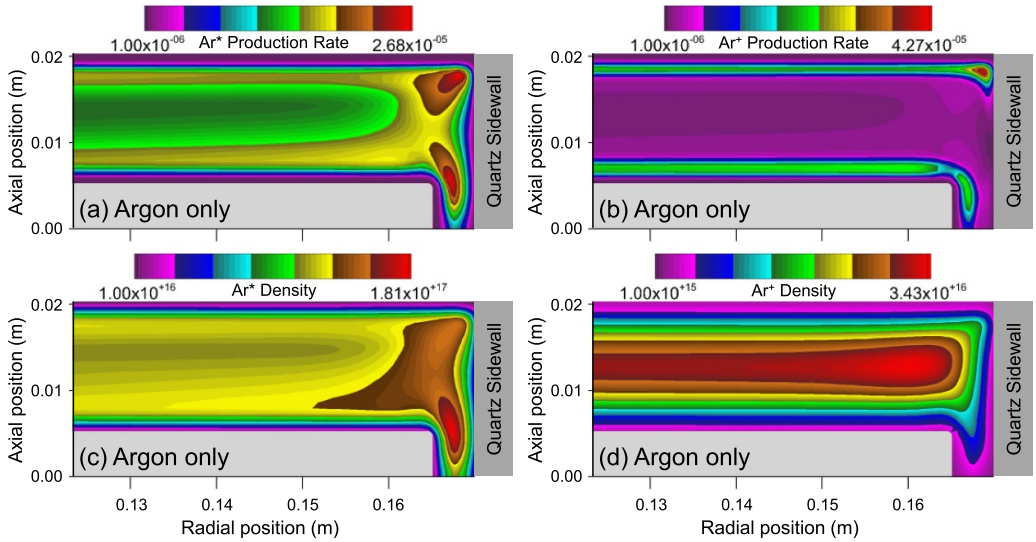

Figure 2. Spatial variations of the time-averaged plasma parameters: (a) excitation rate (kmol m^{-3} s^{-1}), (b) ionization rate (kmol m^{-3} s^{-1}), (c) Ar^* density (m^{-3}), and (d) Ar^+ density (m^{-3}) for Case 1.

the top electrode of the CCP reactor considered in this study is directly connected to the sidewalls. As a result, the electrode edge effects caused by excited species can be clearly observed near the bottom electrode. This is attributed to the existence of only one corner point at the bottom electrode edge. For the case of SiH_4/He, according to figure 3(a), the distribution of the excitation rate between electrodes is fairly symmetrical. Therefore, in figure 3(c), the distribution of excited species (He^*) is also symmetrical in the axial direction. The density of He^* peaks near the electrode edges based on the source function. SiH_4/Ar exhibits a characteristic skew in the profile in figure 3(d) because the peak density of the excited species shifts slightly toward the bottom electrode.

The ionization rate distributions of the dilution gases are displayed in figure 4(a) for the case of SiH_4/He (Case 2) and in figure 4(b) for the case of SiH_4/Ar (Case 3). The ion density distributions of the dilution gases are shown in figure 4(c) for SiH_4/He (Case 2) and in figure 4(d) for SiH_4/Ar (Case 3).

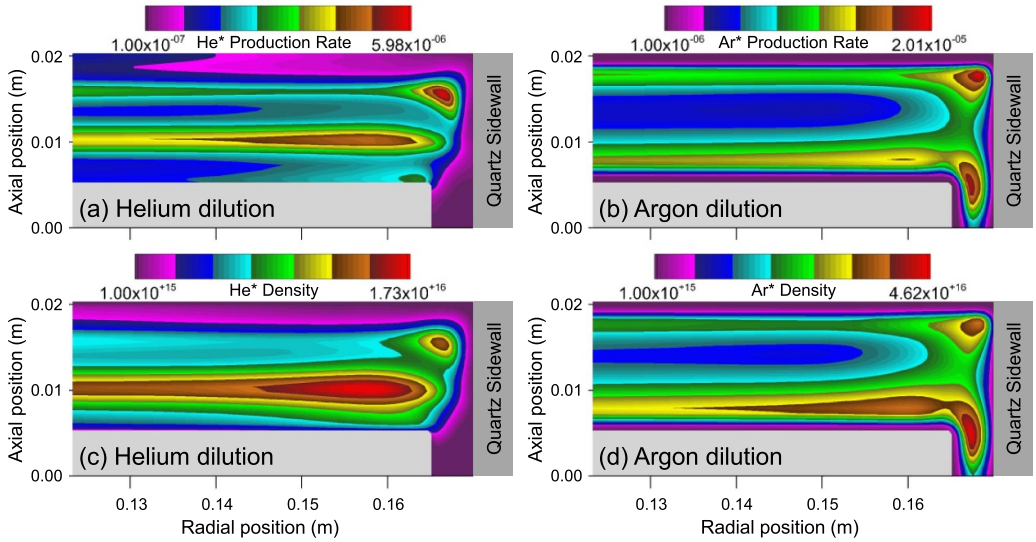

Figure 3. Spatial variations of the time-averaged plasma parameters: (a) He excitation rate (kmol m^{-3} s^{-1}) for Case 2, (b) Ar excitation rate (kmol m^{-3} s^{-1}) for Case 3, (c) He^* density (m^{-3}) for Case 2, and (d) Ar^* density (m^{-3}) for Case 3.

Common to both the He and Ar cases, in figures 4(a) and (b), the ionization rate is observed to increase near the bottom electrode edge, and the characteristic feature of this ionization rate distribution is that it has a distribution skewed axially toward the bottom electrode by the electrons heated in the sheath.

Furthermore, common to both the He and Ar dilutions, the excitation rate profile and the ionization rate profile have very similar distribution characteristics. Electrostatic excitation, which is one of the main sources of metastable species, has a distribution that is essentially similar to that of ionization. The interesting difference is that the axial distribution of the He^+ density has a 'double humped shape,' whereas the axial distribution of the Ar^+ density is 'bell shaped.' Apart from this, Ar^+ has an off-axis maximum that is 2 orders of magnitude higher than that of He^+. This difference in value is attributed to the threshold value of He ionization being about 10 eV higher than that of Ar ionization, and the pressure being considered exceeds 100 Pa in this study.

In addition, we should note that the branching and rate coefficients for the charge-exchange reactions of He^+ with SiH_4 were set as shown below [48]:

$$He^+ + SiH_4 \rightarrow Si^+ + 2H_2 + He,\ k_r = 6.2 \times 10^{-16} m^3 s^{-1}, \quad (14a)$$

$$He^+ + SiH_4 \rightarrow SiH^+ + 3H + He,\ k_r = 3.8 \times 10^{-16} m^3 s^{-1}, \quad (14b)$$

$$He^+ + SiH_4 \rightarrow {SiH_2}^+ + 2H + He,\ k_r = 3.8 \times 10^{-17} m^3 s^{-1}, \quad (14c)$$

$$He^+ + SiH_4 \rightarrow {SiH_3}^+ + H + He,\ k_r = 3.8 \times 10^{-17} m^3 s^{-1}, \quad (14d)$$

where k_r represents the reaction rate coefficient.

Additionally, the branching and rate coefficients for the charge-exchange reactions of Ar^+ with SiH_4 were set as shown below [28, 49]:

$$Ar^+ + SiH_4 \rightarrow Si^+ + H_2 + H_2 + Ar,\ k_r = 1.18 \times 10^{-17} m^3 s^{-1}, \quad (15a)$$

$$Ar^+ + SiH_4 \rightarrow SiH^+ + H + H_2 + Ar,\ k_r = 4.20 \times 10^{-18} m^3 s^{-1}, \quad (15b)$$

$$Ar^+ + SiH_4 \rightarrow {SiH_2}^+ + H_2 + Ar,\ k_r = 1.66 \times 10^{-18} m^3 s^{-1}, \quad (15c)$$

$$Ar^+ + SiH_4 \rightarrow {SiH_3}^+ + H + Ar,\ k_r = 2.40 \times 10^{-18} m^3 s^{-1}, \quad (15d)$$

where k_r represents the reaction rate coefficient.

Considering the reaction rate coefficients mentioned above, it is confirmed that the depletion rate coefficient of He^+ is greater than that of Ar^+. Therefore, because of the larger depletion rate coefficient, He^+ generated near the top electrode and the bottom electrode is not sufficiently transferred to the plasma bulk and is rapidly consumed near the electrodes. As a result, a 'double humped shape' is observed in the He^+ density distribution. On the other hand, because Ar^+ has a small depletion rate coefficient, it is sufficiently delivered to the plasma bulk. As a result, unlike the He^+ density distribution, the Ar^+ density distribution has a 'bell shape'.

Figures 5(a) and (b) display the time-averaged electron density (N_e, m^{-3}) profiles for dilution with He (Case 2) and Ar (Case 3), respectively. The increasing excitation and ionization elevate the electron density when the dilution gas is changed from He to Ar, as shown in figures 5(a) and (b). The electron density increases as a result of electron impact ionization, which is the main process whereby electrons are produced. As long as the input parameters remain the same, the electron density in SiH_4/Ar is higher than that in SiH_4/He. The reason may be that Ar has lower excitation and ionization threshold energies than He. As a consequence of dilution with Ar, the plasma variables are distributed more uniformly despite the higher electron density.

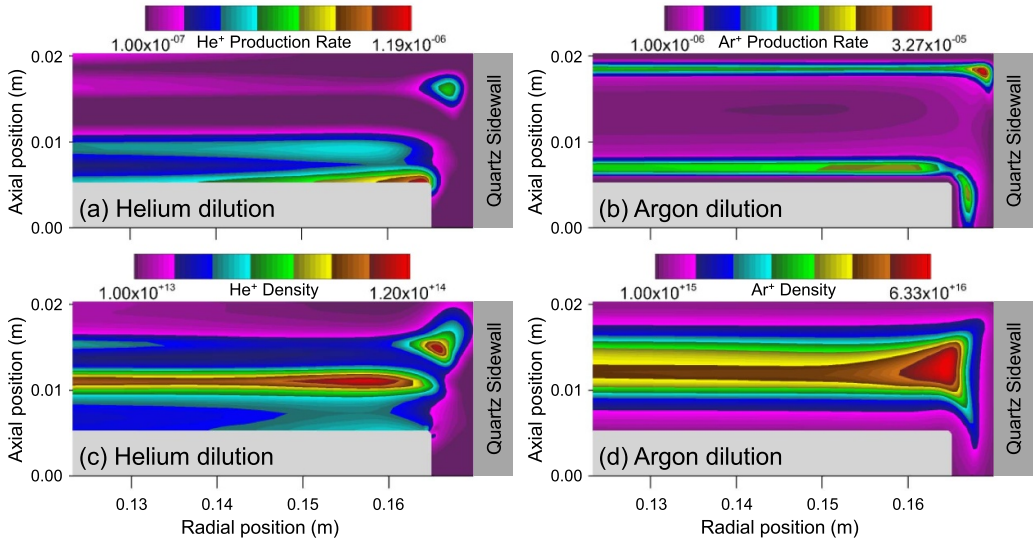

Figure 4. Spatial variations in the time-averaged plasma parameters: (a) He ionization rate (kmol m^{-3} s^{-1}) for Case 2, (b) Ar ionization rate (kmol m^{-3} s^{-1}) for Case 3, (c) He^+ density (m^{-3}) for Case 2, and (d) Ar^+ density (m^{-3}) for Case 3.

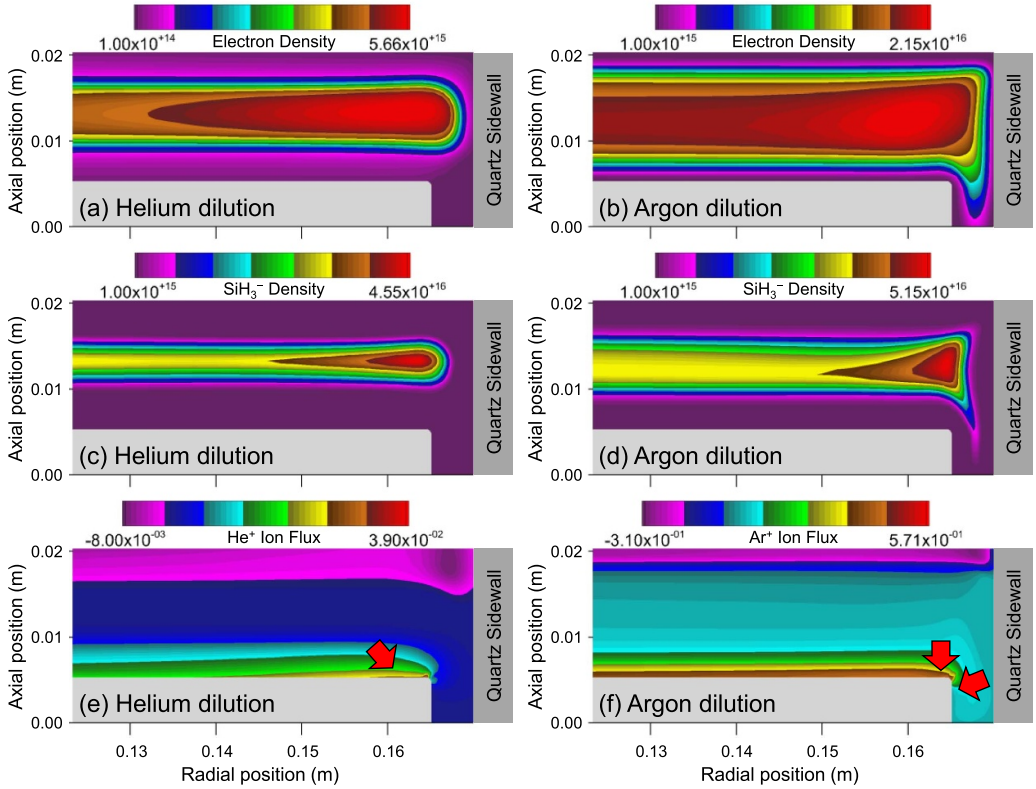

Figure 5. Spatial variations of the time-averaged plasma parameters: (a) N_e (m^{-3}) for Case 2, (b) N_e (m^{-3}) for Case 3, (c) SiH_3^- density (m^{-3}) for Case 2, (d) SiH_3^- density (m^{-3}) for Case 3, (e) axial flux of Ar^+ ion (mA cm^{-2}) for Case 2, and (f) axial flux of He^+ ion (mA cm^{-2}) for Case 3.

Figures 5(c) and (d) display the time-averaged SiH_3^- density (m^{-3}) profiles for dilution with He (Case 2) and Ar (Case 3), respectively. Negative ions including SiH_3^- and SiH_2^- are generated from SiH_4 through dissociative attachment. The negative ion density profile was observed to be more diffuse in both the axial and radial directions as the dilution gas was changed from He to Ar. Because the potential well limits the transport of negative ions due to the low mobility of these ions, the distribution of negative ions is more closely confined to the vicinity of the site at which the negative ions are generated in the case of dilution with He.

Meanwhile, Schulze *et al* found that strongly electronegative discharges exhibit considerable ionization caused by electrons accelerated by strong drift and ambipolar electric fields

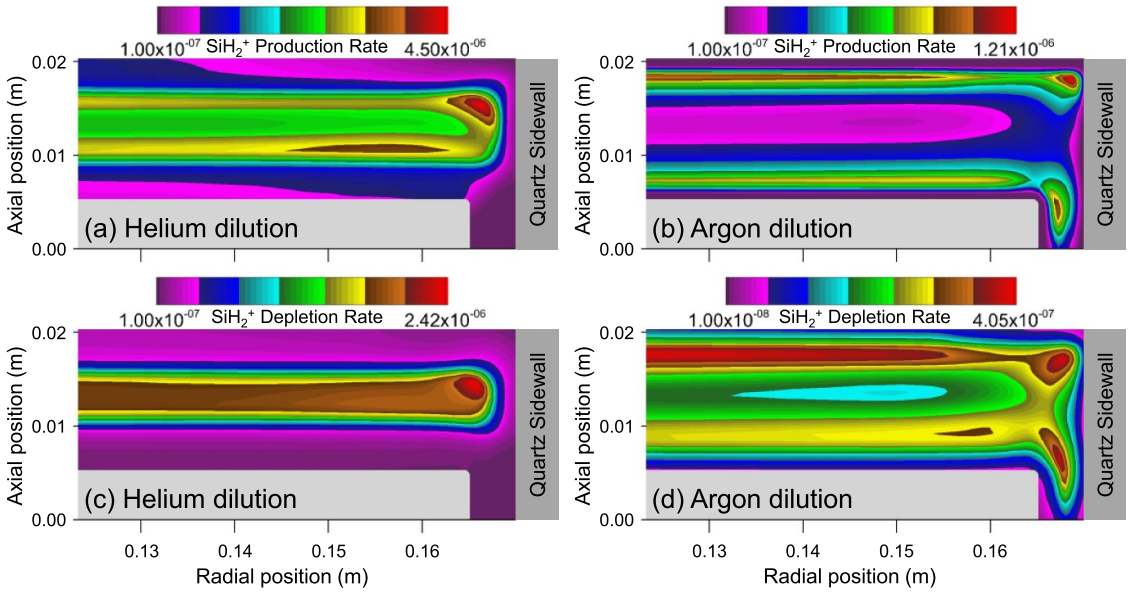

Figure 6. Spatial variations of the time-averaged plasma parameters: (a) SiH_2^+ production rate (kmol m^{-3} s^{-1}) for Case 2, (b) SiH_2^+ production rate (kmol m^{-3} s^{-1}) for Case 3, (c) SiH_2^+ depletion rate (kmol m^{-3} s^{-1}) for Case 2, and (d) SiH_2^+ depletion rate (kmol m^{-3} s^{-1}) for Case 3.

in the plasma bulk [50]. However, our process conditions differ from those of Schulze *et al* in that the gas pressure is high and the proportion of SiH_4 is low: Schulze *et al* used a gas pressure of 40 Pa and pure CF_4. Therefore, the electronegativity is also not relatively high compared to the results for pure SiH_4 discharge or pure CF_4 discharge. Because of these important differences, the results we observed differ from those of Schulze *et al*.

Another important consideration is that the electron density and electron mean energy in combination determine the ionization rate, since the electron mean energy can be used to determine the ionization rate coefficient. A higher ion flux (mA cm^{-2}) near the electrode edge is correlated with a higher electron mean energy. Accordingly, higher corner rates are strongly correlated with greater ion fluxes, as can be seen in figures 5(e) and (f) for He dilution and Ar dilution, respectively. Therefore, when observing the distribution of the ion flux, the excitation and ionization rates in the case of Ar dilution are understood to have a distribution biased toward the bottom electrode. The distribution of the ion flux in Ar is also observed to be more uniform in the radial direction.

3.2. *Effects of dilution gas on the spatial variation of the plasma parameters related to ionic species of SiH_4*

The effect of the dilution gas on the plasma parameters related to the SiH_2^+ and SiH_3^+ ions are considered in this section. The time-averaged ionization rate profiles (the production of SiH_2^+: $e^- + SiH_4 \rightarrow SiH_2^+ + H + H + e^- + e^-$) for He dilution (Case 2) and for Ar dilution (Case 3) are depicted in figures 6(a) and (b), respectively. The time-averaged depletion rate profiles (the depletion of SiH_2^+: $SiH_2^+ + SiH_4 \rightarrow SiH_3^+ + SiH_3$) for He dilution (Case 2) and for Ar dilution (Case 3) are presented in figures 6(c) and (d), respectively.

Dilution with He gives rise to significantly enhanced ionization rates near both the top and bottom electrode edges; thus, the radial distribution of these rates is non-uniform in figure 6(a). Substantial local enhancement occurs, particularly between the top electrode edge and the top sidewall. As shown in figure 6(b), when Ar is used as diluent, the ionization rates near the bottom electrode edge are not uniform within the axial profile. The peak ionization rate in the inter-electrode region is lower and shifts only toward the bottom electrode for Ar dilution. Additionally, the ionization rates peak near the edge at which the bottom electrode is located, but they are relatively lower and distributed uniformly at $r \leqslant 130$ mm in the case of Ar dilution.

In a similar manner to figures 6(a) and (b), figures 6(c) and (d) demonstrate that the depletion rates are also enhanced and localized near the electrode edge, and are therefore not uniformly distributed radially, neither for He nor for Ar dilution, respectively.

In figures 7(a) and (b), we show the time-averaged SiH_3^+ density profiles for He dilution (Case 2) and Ar dilution (Case 3). Figures 7(c) and (d) show the time-averaged SiH_2^+ density profiles for dilution with He (Case 2) and Ar (Case 3). As can be seen from these contours, SiH_3^+ is the dominant ion. The SiH_3^+ density peaks at an order of magnitude higher than the SiH_2^+ density under the examined discharge conditions. In the case of Ar dilution, a greater difference between SiH_3^+ and SiH_2^+ appears, particularly in the midplane of the discharge. In addition, for dilution with Ar, the axial density profiles of SiH_3^+ are quite different from those of SiH_2^+, and this difference is similar to that evident from the ionization rate profiles

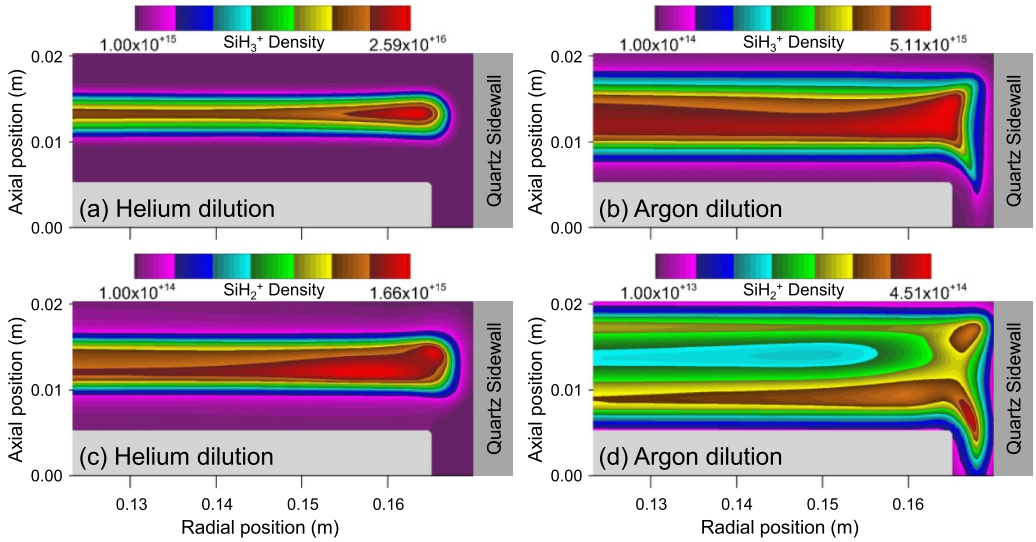

Figure 7. Spatial variations of the time-averaged plasma parameters: (a) SiH_3^+ density (m^{-3}) for Case 2, (b) SiH_3^+ density (m^{-3}) for Case 3, (c) SiH_2^+ density (m^{-3}) for Case 2, and (d) SiH_2^+ density (m^{-3}) for Case 3.

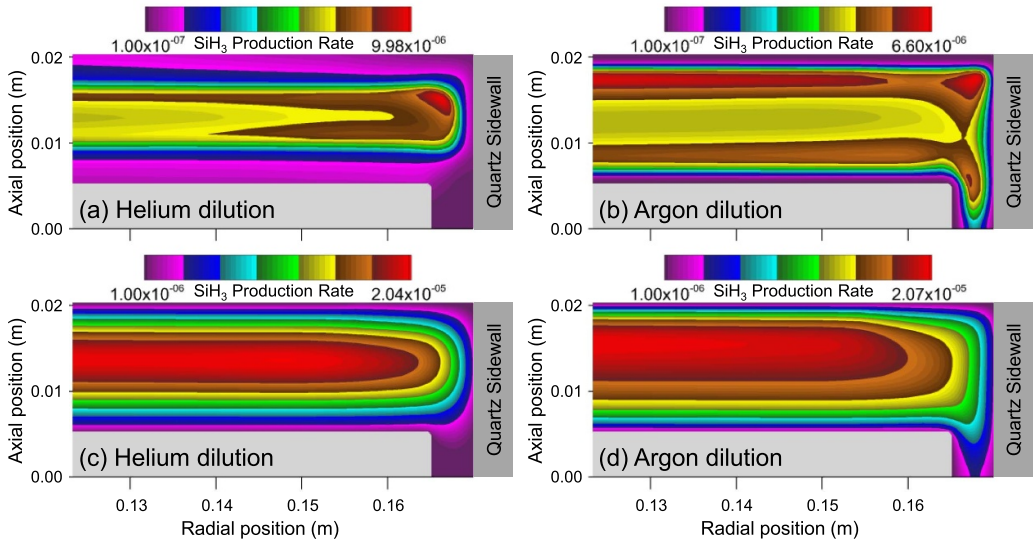

Figure 8. Spatial variations in the time-averaged neutral transport parameters. SiH_3 production rates (kmol m^{-3} s^{-1}) by electron impact dissociation for (a) Case 2, and (b) Case 3. SiH_3 production rates (kmol m^{-3} s^{-1}) by the hydrogen abstraction reaction for (c) Case 2, and (d) Case 3.

in figure 6(b). In the case of SiH_2^+, ion consumption in the gas phase occurs rapidly via the secondary ion conversion reaction involving SiH_2^+, whereas SiH_3^+ diffusion from the bulk to the sheath is followed by drift transport through the sheath and neutralization at the electrode surfaces. Because of this, the density profile of SiH_3^+ is smooth with a maximum at the center of the discharge, whereas the peak value for SiH_2^+ can be observed where the production of these ions is the highest. In addition, in the case of Ar dilution, the fluxes of SiH_3^+ towards the electrodes and throughout the discharge are lower.

In summary, figures 6 and 7 indicate that the density distribution characteristic of the SiH_4 ions is significantly affected by the dilution gas. Since the ion collision rate increases with Ar dilution, the mean free path is decreased for the ions. The reduction of the loss rates at the electrodes increases the ion and electron density, resulting in the sheath width becoming narrower.

3.3. Effects of the dilution gas on the spatial distributions of the neutral transport parameters

The impact of the dilution gas on the spatial distribution of the neutral transport parameters is discussed in this section. Considering that the distribution of a-Si:H is influenced by SiH_3, it was selected for the purpose of analyzing the transport of neutral species. The time-averaged production rate profiles resulting from electron impact dissociation ($e^- + SiH_4 \rightarrow SiH_3 + H + e^-$) for He (Case 2) and Ar dilution (Case 3) are depicted in figures 8(a) and (b), respectively. In addition, the time-averaged production rate profiles by hydrogen

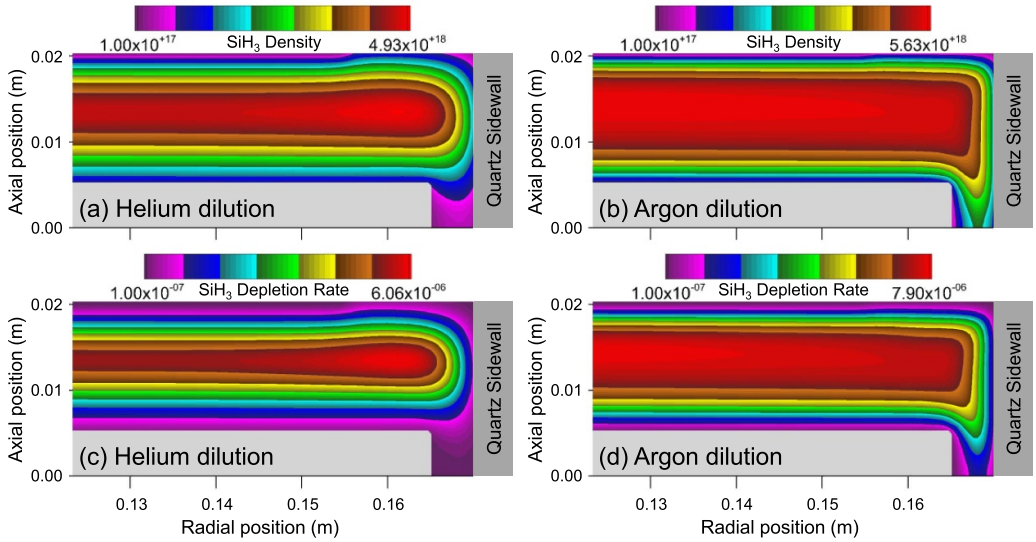

Figure 9. Spatial profiles of the time-averaged neutral transport parameters: (a) SiH_3 density (m^{-3}) for Case 2, (b) SiH_3 density (m^{-3}) for Case 3, (c) SiH_3 depletion rate ($SiH_3 + SiH_3 \rightarrow SiH_2 + SiH_4$; kmol m^{-3} s^{-1}) for Case 2, and (d) SiH_3 depletion rate ($SiH_3 + SiH_3 \rightarrow SiH_2 + SiH_4$; kmol m^{-3} s^{-1}) for Case 3.

abstraction ($SiH_4 + H \rightarrow H_2 + SiH_3$) for He dilution (Case 2) and Ar dilution (Case 3) are depicted in figures 8(c) and (d), respectively.

According to figure 8(a), the reaction rates in Case 2 are significantly elevated at both the top electrode and bottom electrode edges, and are therefore distributed in a non-uniform manner. However, as observed in figure 8(b), the spatial distribution of the SiH_3 production rate in the case of Ar dilution is relatively less focused on the edge. This is judged to reflect the difference in the electron density distribution. However, the spatial distributions of the SiH_3 production rate by hydrogen abstraction (figures 8(c) and (d)) have 'bulk dominant' distribution in common regardless of the dilution gas.

Figures 9(a) and (b) show the spatial variations in the SiH_3 densities (m^{-3}) for Case 2 and Case 3, respectively. Considering that SiH_3 production is mainly governed by electron impact dissociation with low threshold energy and hydrogen abstraction, Ar dilution would be expected to produce more radicals such as those of SiH_3 and H. Comparing figures 9(a) with (b) reveals that the SiH_3 density clearly increases with Ar dilution. Importantly, the off-axis maximum is not observed in the spatial distribution of the SiH_3 density in the case of Ar dilution.

Additionally, as observed in figures 9(c) and (d), the SiH_3 depletion rate is more distributed in the case of Ar dilution. The enhancement of the disproportionation process in the case of Ar dilution has the effect of rapidly depleting the SiH_3 in the bulk:

$$SiH_3 + SiH_3 \rightarrow SiH_2 + SiH_4. \quad (16)$$

Based on equation (4), the reduced diffusion coefficient of SiH_3 can also induce local accumulation in the case of Ar dilution. The density distributions of neutral species could undergo marked axial variation when local depletion is increased and the diffusion coefficient is decreased in the case of Ar dilution. As a result, the density near both the top and bottom surfaces is lowered, resulting in fast SiH_3 loss in the bulk. Therefore, Ar dilution enhances the axial variations in the density distributions, as shown in figure 9.

Figures 10(a) and (b) show the spatial variations in the Si_2H_6 densities (m^{-3}) for He (Case 2) and Ar dilution (Case 3), respectively. As Ar dilution accelerates the gas phase reaction, SiH_4 is depleted rapidly, which, in turn, leads to the fast production of Si_2H_6 in the gas phase. As a result, the concentration of Si_2H_6 observed in the inter-electrode region in the case of Ar dilution is observed to be approximately ten times higher than the concentration of Si_2H_6 in the case of He dilution. This high concentration plays a determinant role in governing the formation of important radicals that determine the deposition rate and in determining the difference in the deposition rate profiles for Ar dilution and He dilution. Because the concentration of Si_2H_6 is higher in the case of Ar dilution, the rate at which Si_2H_5 is produced (formed by the hydrogen abstraction of Si_2H_6) is higher in the case of Ar dilution, as shown in figures 10(c) and (d).

Figures 11(a) and (b) show the spatial variations in the Si_2H_5 densities (m^{-3}) for Case 2 and Case 3, respectively. As predicted on the basis of the results in figure 10, the density of Si_2H_5 has a higher distribution in the case of Ar dilution. In addition, figures 11(c) and (d) show the spatial variations in the Si_5H_{12} densities (m^{-3}) for Case 2 and Case 3, respectively. In figures 11(c) and (d), He dilution reduces the efficiency of Si_5H_{12} generation, and as a result, the Si_5H_{12} reaches the bottom electrode surface less readily. As Si_5H_{12} approaches the bulk plasma region, its density distribution is commonly observed to increase regardless of the dilution gas. He dilution results in a slight increase in the thickness of the diffusion layers near the showerhead inlet.

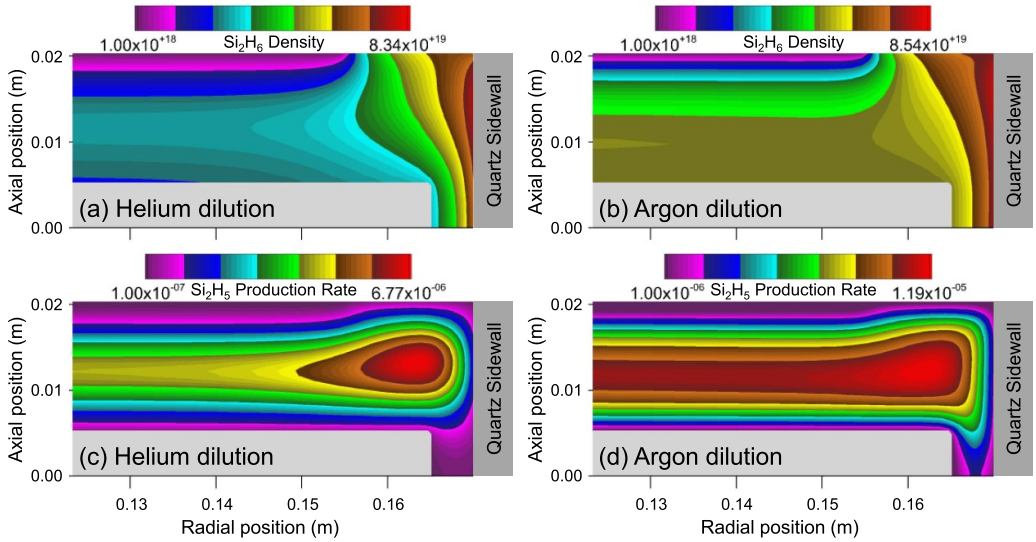

Figure 10. Spatial profiles of the time-averaged neutral transport parameters: (a) SiH_3 density (m^{-3}) for Case 2, (b) SiH_3 density (m^{-3}) for Case 3, (c) Si_2H_5 production rate ($Si_2H_6 + H \rightarrow Si_2H_5 + H_2$; kmol m^{-3} s^{-1}) for Case 2, and (d) Si_2H_5 production rate ($Si_2H_6 + H \rightarrow Si_2H_5 + H_2$; kmol m^{-3} s^{-1}) for Case 3.

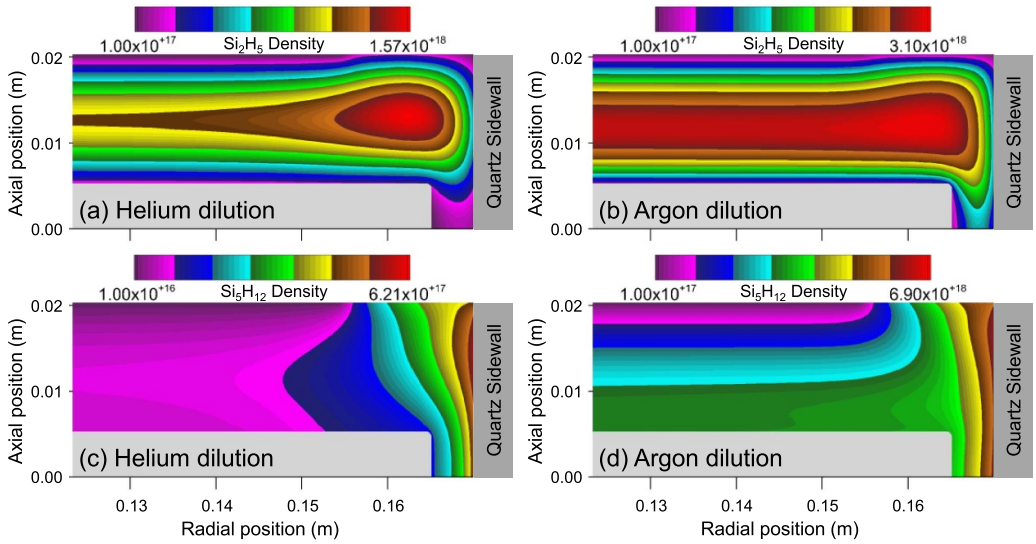

Figure 11. Spatial profiles of the time-averaged neutral transport parameters: (a) Si_2H_5 density (m^{-3}) for Case 2, (b) Si_2H_5 density (m^{-3}) for Case 3, (c) Si_5H_{12} density (m^{-3}) for Case 2, and (d) Si_5H_{12} density (m^{-3}) for Case 3.

Figure 12 compares the deposition rate profiles for dilution with He (Case 2) and Ar (Case 3). The deposition rate profiles are normalized with their corresponding averaged values, and they correspond well with the experimental data. Upon examination of the effect of the dilution gas on the deposition rate profile, we found that, in the case of Ar dilution, the deposition rate profile was nearly 100% more uniform and the deposition rate approximately 87% higher than for He dilution. It is worthy to note that Ar dilution has a higher deposition rate and the deposition rate profile has higher uniformity than that using He dilution. Regarding the process results, Ar dilution delivers superior performance, although He dilution results in a lower density of Si_5H_{12}, as observed in figure 11. This means that when using He dilution, the process result could be safer with respect to particle contamination.

3.4. Effect of the dilution gas on the plasma distributions caused by the input power

In this section, we consider the extent to which and manner in which the spatial distribution of the plasma parameters varies as the input power is increased, depending on whether He or Ar is used for dilution. Figures 13(a) and (b) show the spatial variations in the ionization rates (kmol m^{-3} s^{-1}) as the input power increases from 200 W to 400 W, for dilution with He (Case 4) and for dilution with Ar (Case 5),

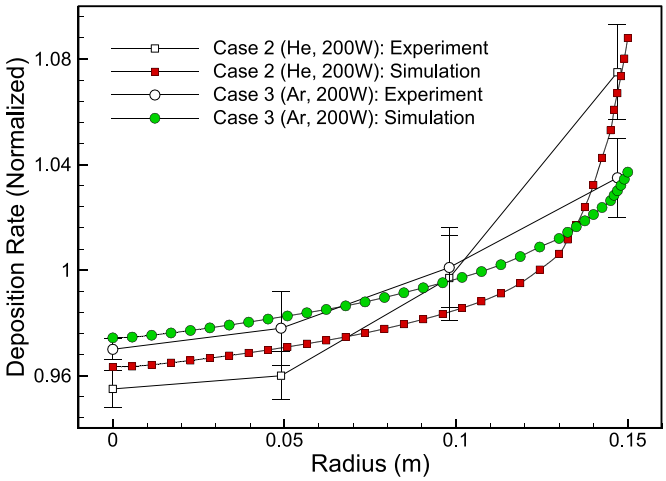

Figure 12. Effect of the dilution gas on the deposition rates. The deposition rate profiles for Case 2 and Case 3 are plotted. The experimental data of Case 2 and Case 3 are superimposed.

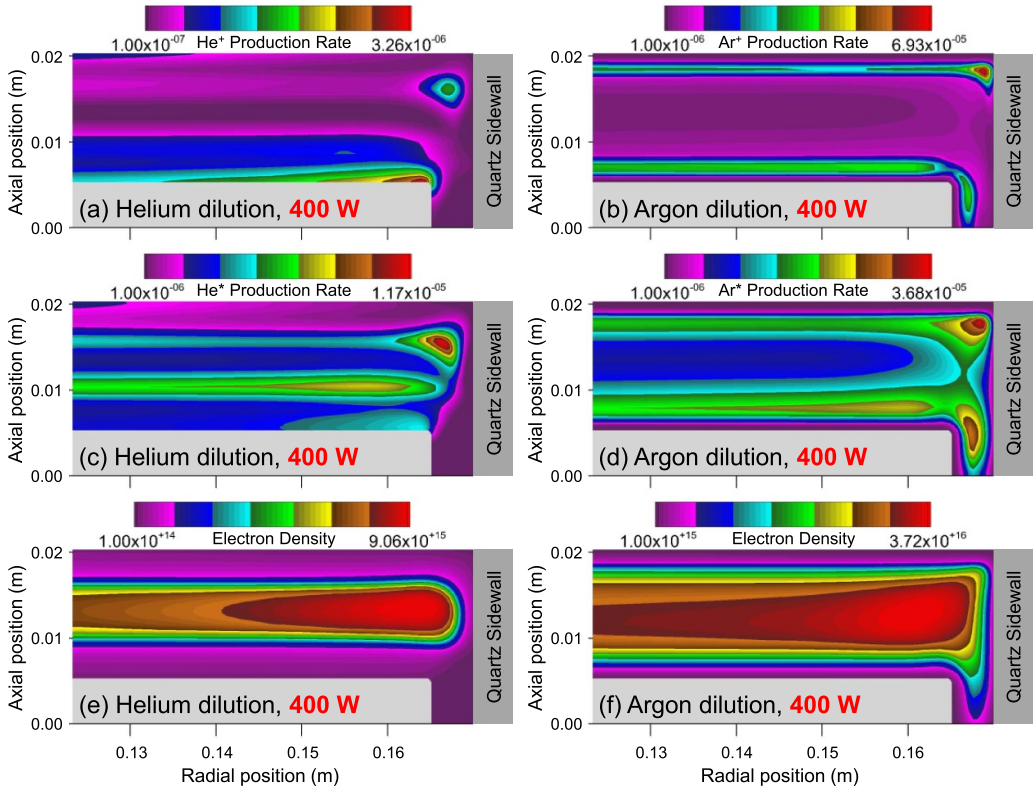

Figure 13. Spatial variations of the time-averaged plasma parameters: (a) ionization rate (kmol m^{-3} s^{-1}) for Case 4, (b) ionization rate (kmol m^{-3} s^{-1}) for Case 5, (c) excitation rate (kmol m^{-3} s^{-1}) for Case 4, (d) excitation rate (kmol m^{-3} s^{-1}) for Case 5, (e) electron density (m^{-3}) for Case 4, and (f) electron density (m^{-3}) for Case 5.

respectively. An increase in the input power is accompanied by an increase in the RF voltage (V_{rf}). As the peak voltage increases, the resulting peak value of the plasma potential formed near the sheath also increases. Analysis of the corresponding change in the ionization rate following adjustment of the peak voltage revealed that an increase in the peak voltage leads to an increase in the maximum value of the ionization rate. The electrons gain energy by interacting with the stronger electric field near the sheath due to the plasma potential caused by the elevated peak voltage. This higher energy is associated with a higher electron temperature.

As a result, electron heating becomes more efficient, and consequently, the electrons have more kinetic energy, i.e., the electron temperature increases. Because the ionization rate is mainly expressed as a function of electron temperature, the ionization rate increases as the electron temperature increases. Therefore, by increasing the input power from 200 W to 400 W, the peak value of the ionization rate increases from

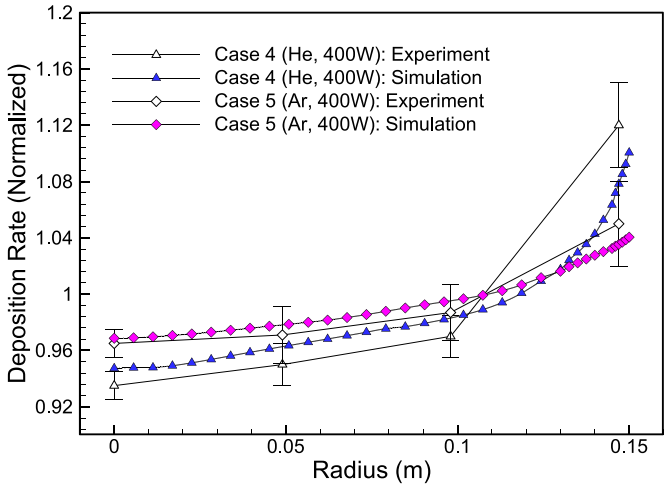

Figure 14. Effect of the dilution gas on the deposition rates. The deposition rate profiles for Case 4 and Case 5 are plotted. The experimental data of Case 4 and Case 5 are superimposed.

1.19×10^{-6} kmol m^{-3} s^{-1} to 3.26×10^{-6} kmol m^{-3} s^{-1} in the case of He dilution, whereas the peak values of the ionization rate increase from 3.27×10^{-5} kmol m^{-3} s^{-1} to 6.93×10^{-5} kmol m^{-3} s^{-1} in the case of Ar dilution.

Moreover, the excitation rate also increases with the peak voltage, as shown in figure 13(c) for He dilution and in figure 13(d) for Ar dilution. Ultimately, higher input power increases the electron collisions with other species, and, in turn, this promotes electron impact reactions. Thus, the most important effect of increasing the input power (or voltage) is its influence on elevating the electron density, as depicted in figure (e) for the case of He dilution and in figure (f) for the c ase of Ar dilution. At 400 W, the peak electron density reaches 9.06×10^{15} m^{-3} for He dilution and 3.72×10^{16} m^{-3} for Ar dilution.

Importantly, for He dilution, an increase in power causes the density distribution of the electrons to become less uniform because local heating near the electrode edge is enhanced by the higher input power. Because the spatial distribution of the plasma parameters is relatively less uniform for He dilution, as a result, the deposition rate profile for He dilution in figure 14 is considerably less uniform than that for Ar dilution. Furthermore, in the case of Ar dilution, even when the input power is 400 W, the uniformity of the deposition rate profile does not change significantly relative to the RF power of 200 W, but the edge profile rises more severely in the case of He dilution. In the case of Ar dilution, the deposition rate profile was about 113% more uniform and the deposition rate approximately 90% higher than for He dilution. Finally, the results in figure 14 confirm that the experimental and simulated values are in good agreement even when the RF power was adjusted to 400 W.

4. Discussions

In this study, we numerically computed the difference in the spatial distribution of the plasma parameters between SiH_4/He mixture CCP and SiH_4/Ar mixture CCP using a 2D fluid model. The results presented in this paper indicate that the excited species moved towards the bottom electrode and are skewed toward the corner in the case of Ar dilution. The skewness was principally determined by the shortening of the electron mean free paths (due to the higher collision frequency in the case of Ar dilution) and the increase in Ar^* quenching due to the higher electron density and the related reaction rate coefficient. In the case of He dilution, the skewness was observed to have formed in the spatial distribution of the He^* density, but the skewness was less prominent compared to the case of Ar dilution under the same process conditions. This relative difference arises because, with Ar dilution, the electron mean free path is shorter and the electron density is higher than in the case of He dilution.

As a result, electrons located near the electrode and heated by the plasma sheath can dissipate their energy by excitation closer to the electrode in the case of Ar dilution. The higher electron density for Ar dilution results in a thinner sheath. A greater electric field enhancement is observed along the electrode edge when the sheath collapses. This enlarges the skewness of the Ar^* density profile. The collapsing sheath form resulting from an increase in the power deposition in the case of Ar dilution has sufficient short mean free paths to affect the Ar^* source function. The higher plasma density also increases Ar^* quenching. This increase restricts the Ar^* to nearer the source of generation, and thus confines the Ar^* closer to its location. However, despite this elevated skewness, the distribution of the plasma parameters in the radial direction near the bottom electrode is more uniform in the case of Ar dilution. As a result, the deposition rate profile in the case of Ar dilution was found to be more uniform than that in the case of He dilution, regardless of the change in input power.

5. Conclusions

Our study was concerned with modeling the difference in the spatial distribution of the plasma parameters between SiH_4/He CCP and SiH_4/Ar CCP. The SiH_4/He CCP process was modeled using the chemical reaction model of the SiH_4/He mixture we developed and successfully applied in previous studies. The chemical reaction model of the SiH_4/Ar mixture was built in this study and is based on the detailed chemical reaction set of Ar. The spatial distribution of the plasma parameters was studied by conducting 2D fluid modeling, whereupon the simulation results of the chemical reactions in the plasma were used to numerically analyze the deposition of a hydrogenated amorphous silicon film.

The results presented in this paper show that the excited species moved toward the bottom electrode and were skewed toward the corner in the case of Ar dilution. Skewness was also observed in the case of He dilution, but the skewness was relatively less obvious compared to Ar dilution under the same process conditions. In addition, as a change in the dilution gas was shown to enhance the growth rate and improve the uniformity of the deposition profile, the effects of the dilution gas were clarified in this study. The results showed that Ar

dilution leads to more uniform ionization and excitation rates and thus more uniform density distributions of ions and radicals. Investigation of the effect of the dilution gas on the deposition rate profile for an input power of 200 W confirmed that the deposition rate profile for Ar dilution was approximately 100% more uniform than that for dilution with He. In addition, the deposition rate for Ar dilution was about 87% higher. The numerical results were in good correspondence with the results of our experiments.

Finally, we determined the extent to which and the manner in which the spatial distribution of the plasma parameters changed for dilution with He and Ar by increasing the RF power from 200 W to 400 W. For dilution with Ar, even when the RF power is doubled to 400 W, the uniformity of the deposition rate profile does not change significantly; however, in the case of He dilution, the edge profile rises more severely.

Data availability statements

The data cannot be made publicly available upon publication because the cost of preparing, depositing and hosting the data would be prohibitive within the terms of this research project. The data that support the findings of this study are available upon reasonable request from the authors.

Acknowledgments

This work was supported by the research fund of Hanyang University (HY-2022-3095). This work was supported by the National Research Council of Science & Technology (NST) grant by the Korea government (MSIT) (No. CRC-20-01-NFRI). This work was supported by Soonchunhyang University Research Fund. This work was supported by Korea Institute for Advancement of Technology(KIAT) grant funded by Korea Government (MOTIE) (P0020612, 2023 The Competency Development Program for Industry Specialist).

Appendix

For brevity of notation, table A1 in the appendix lists the remaining gas phase reactions.

Table A1. Remaining gas-phase reactions considered in this study. The units of T_e and T_g in the rate coefficients are eV and K, respectively.

Index	Reactions	Cross section or Rate coefficient	
	Ar reactions	(m^3 s^{-1}), (m^6 s^{-1}), or (s^{-1})	References
AR01	$e^- + Ar \rightarrow e^- + Ar$	Cross section, $\sigma(\varepsilon)$	[33, 51, 52]
AR02	$e^- + Ar \rightarrow 2e^- + Ar^+$	Cross section, $\sigma(\varepsilon)$	[33, 51, 52]
AR03	$e^- + Ar \rightarrow e^- + Ar(^3P_2)$	Cross section, $\sigma(\varepsilon)$	[33, 53, 54]
AR04	$e^- + Ar \rightarrow e^- + Ar(^3P_1)$	Cross section, $\sigma(\varepsilon)$	[33, 53, 54]
AR05	$e^- + Ar \rightarrow e^- + Ar(^3P_0)$	Cross section, $\sigma(\varepsilon)$	[33, 53, 54]
AR06	$e^- + Ar \rightarrow e^- + Ar(^1P_1)$	Cross section, $\sigma(\varepsilon)$	[33, 53, 54]
AR07	$e^- + Ar \rightarrow e^- + Ar(4p)$	Cross section, $\sigma(\varepsilon)$	[33, 53, 55]
AR08	$e^- + Ar(^3P_2) \rightarrow e^- + Ar$	$4.30 \times 10^{-16}\ T_e^{0.74}$	[33, 56]
AR09	$e^- + Ar(^3P_1) \rightarrow e^- + Ar$	$4.30 \times 10^{-16}\ T_e^{0.74}$	[33, 56]
AR10	$e^- + Ar(^3P_0) \rightarrow e^- + Ar$	$4.30 \times 10^{-16}\ T_e^{0.74}$	[33, 56]
AR11	$e^- + Ar(^1P_1) \rightarrow e^- + Ar$	$4.30 \times 10^{-16}\ T_e^{0.74}$	[33, 56]
AR12	$e^- + Ar(4p) \rightarrow e^- + Ar$	$3.90 \times 10^{-16}\ T_e^{0.71}$	[33, 56]
AR13	$e^- + Ar(^3P_2) \rightarrow 2e^- + Ar^+$	Cross section, $\sigma(\varepsilon)$	[33, 56, 57]
AR14	$e^- + Ar(^3P_1) \rightarrow 2e^- + Ar^+$	Cross section, $\sigma(\varepsilon)$	[33, 56, 57]
AR15	$e^- + Ar(^3P_0) \rightarrow 2e^- + Ar^+$	Cross section, $\sigma(\varepsilon)$	[33, 56, 57]
AR16	$e^- + Ar(^1P_1) \rightarrow 2e^- + Ar^+$	Cross section, $\sigma(\varepsilon)$	[33, 56, 57]
AR17	$e^- + Ar(4p) \rightarrow 2e^- + Ar^+$	Cross section, $\sigma(\varepsilon)$	[33, 56, 57]
AR18	$e^- + Ar(^3P_2) \rightarrow e^- + Ar(4p)$	Cross section, $\sigma(\varepsilon)$	[33, 56, 57]
AR19	$e^- + Ar(^3P_1) \rightarrow e^- + Ar(4p)$	Cross section, $\sigma(\varepsilon)$	[33, 56, 57]
AR20	$e^- + Ar(^3P_0) \rightarrow e^- + Ar(4p)$	Cross section, $\sigma(\varepsilon)$	[33, 56, 57]
AR21	$e^- + Ar(^1P_1) \rightarrow e^- + Ar(4p)$	Cross section, $\sigma(\varepsilon)$	[33, 56, 57]
AR22	$e^- + Ar(4p) \rightarrow e^- + Ar(^3P_2)$	$3.00 \times 10^{-13}\ T_e^{0.51} \times 0.25$	[33, 56]
AR23	$e^- + Ar(4p) \rightarrow e^- + Ar(^3P_1)$	$3.00 \times 10^{-13}\ T_e^{0.51} \times 0.25$	[33, 56]
AR24	$e^- + Ar(4p) \rightarrow e^- + Ar(^3P_0)$	$3.00 \times 10^{-13}\ T_e^{0.51} \times 0.25$	[33, 56]
AR25	$e^- + Ar(4p) \rightarrow e^- + Ar(^1P_1)$	$3.00 \times 10^{-13}\ T_e^{0.51} \times 0.25$	[33, 56]
AR26	$e^- + Ar(^3P_2) \rightarrow e^- + Ar(^3P_1)$	$2.00 \times 10^{-13} \times 0.5$	[33, 56]
AR27	$e^- + Ar(^3P_2) \rightarrow e^- + Ar(^1P_1)$	$2.00 \times 10^{-13} \times 0.5$	[33, 56]
AR28	$e^- + Ar(^3P_0) \rightarrow e^- + Ar(^3P_1)$	$2.00 \times 10^{-13} \times 0.5$	[33, 56]
AR29	$e^- + Ar(^3P_0) \rightarrow e^- + Ar(^1P_1)$	$2.00 \times 10^{-13} \times 0.5$	[33, 56]
AR30	$2e^- + Ar^+ \rightarrow e^- + Ar$	$10^{-31} \times (T_e \times 38.696)^{-4.5}$	[33, 58]
AR31	$e^- + Ar(^3P_1) \rightarrow e^- + Ar(^3P_2)$	$9.10 \times 10^{-13} \times 0.5$	[33, 59]
AR32	$e^- + Ar(^3P_1) \rightarrow e^- + Ar(^3P_0)$	$9.10 \times 10^{-13} \times 0.5$	[33, 59]
AR33	$e^- + Ar(^1P_1) \rightarrow e^- + Ar(^3P_2)$	$9.10 \times 10^{-13} \times 0.5$	[33, 59]
AR34	$e^- + Ar(^1P_1) \rightarrow e^- + Ar(^3P_0)$	$9.10 \times 10^{-13} \times 0.5$	[33, 59]
AR35	$e^- + Ar_2^* \rightarrow 2e^- + Ar_2^+$	Cross section, $\sigma(\varepsilon)$	[33, 57, 60]
AR36	$e^- + Ar_2^+ \rightarrow Ar + Ar(^3P_2)$	$0.60 \times 10^{-12}\ (T_e \times 38.696)^{-0.66} \times 0.25$	[33, 57]
AR37	$e^- + Ar_2^+ \rightarrow Ar + Ar(^3P_1)$	$0.60 \times 10^{-12}\ (T_e \times 38.696)^{-0.66} \times 0.25$	[33, 57]
AR38	$e^- + Ar_2^+ \rightarrow Ar + Ar(^3P_0)$	$0.60 \times 10^{-12}\ (T_e \times 38.696)^{-0.66} \times 0.25$	[33, 57]
AR39	$e^- + Ar_2^+ \rightarrow Ar + Ar(^1P_1)$	$0.60 \times 10^{-12}\ (T_e \times 38.696)^{-0.66} \times 0.25$	[33, 57]
AR40	$e^- + Ar_2^+ \rightarrow Ar + Ar(4p)$	1.10×10^{-13}	[33, 57]
AR41	$e^- + Ar_2^* \rightarrow e^- + 2Ar$	1.00×10^{-13}	[33, 57]
AR42	$2e^- + Ar^+ \rightarrow e^- + Ar(4p)$	$5.00 \times 10^{-39}\ T_e^{-4.5}$	[33, 61]
AR43	$Ar(^3P_1) \rightarrow Ar$	3.00×10^7	[33, 56]
AR44	$Ar(^1P_1) \rightarrow Ar$	3.00×10^7	[33, 56]
AR45	$Ar(4p) \rightarrow Ar$	3.20×10^7	[33, 56]
AR46	$e^- + Ar^+ \rightarrow Ar(^3P_2)$	$10^{-17} \times 0.5$	[33, 62]
AR47	$e^- + Ar^+ \rightarrow Ar(^3P_0)$	$10^{-17} \times 0.5$	[33, 62]
AR48	$e^- + Ar^+ \rightarrow Ar(4p)$	$4.00 \times 10^{-19}\ T_e^{-0.5}$	[33, 61]
AR49	$Ar(4p) \rightarrow Ar(^3P_2)$	$3.00 \times 10^7 \times 0.5$	[33, 59]
AR50	$Ar(4p) \rightarrow Ar(^3P_0)$	$3.00 \times 10^7 \times 0.5$	[33, 59]
AR51	$Ar(4p) \rightarrow Ar(^3P_1)$	$3.00 \times 10^7 \times 0.5$	[33, 59]
AR52	$Ar(4p) \rightarrow Ar(^1P_1)$	$3.00 \times 10^7 \times 0.5$	[33, 59]
AR53	$Ar_2^* \rightarrow 2Ar$	6.00×10^7	[33, 57]
AR54	$2Ar(^3P_2) \rightarrow e^- + Ar + Ar^+$	6.40×10^{-16}	[33, 58]
AR55	$Ar(^3P_2) + Ar(^3P_0) \rightarrow e^- + Ar + Ar^+$	$6.40 \times 10^{-16} \times 2$	[33, 58]
AR56	$2Ar(^3P_0) \rightarrow e^- + Ar + Ar^+$	6.40×10^{-16}	[33, 58]

(Continued.)

Table A1. (Continued.)

Index	Reactions	Cross section or Rate coefficient	
	Ar reactions	(m^3 s^{-1}), (m^6 s^{-1}), or (s^{-1})	References
AR57	$Ar(^3P_2) + Ar \rightarrow 2Ar$	2.30×10^{-21}	[33, 58]
AR58	$Ar(^3P_0) + Ar \rightarrow 2Ar$	2.30×10^{-21}	[33, 58]
AR59	$Ar(^3P_2) + 2Ar \rightarrow Ar + Ar_2^*$	1.40×10^{-44}	[33, 58]
AR60	$Ar(^3P_0) + 2Ar \rightarrow Ar + Ar_2^*$	1.40×10^{-44}	[33, 58]
AR61	$Ar(^3P_1) + 2Ar \rightarrow Ar + Ar_2^*$	1.14×10^{-44}	[33, 57]
AR62	$Ar(^1P_1) + 2Ar \rightarrow Ar + Ar_2^*$	1.14×10^{-44}	[33, 57]
AR63	$Ar(^3P_2) + Ar(^3P_1) \rightarrow e^- + Ar + Ar^+$	2.10×10^{-15}	[33, 63]
AR64	$Ar(^3P_2) + Ar(^1P_1) \rightarrow e^- + Ar + Ar^+$	2.10×10^{-15}	[33, 63]
AR65	$Ar(^3P_0) + Ar(^3P_1) \rightarrow e^- + Ar + Ar^+$	2.10×10^{-15}	[33, 63]
AR66	$Ar(^3P_0) + Ar(^1P_1) \rightarrow e^- + Ar + Ar^+$	2.10×10^{-15}	[33, 63]
AR67	$2Ar(4p) \rightarrow e^- + Ar + Ar^+$	5.00×10^{-16} $(T_g/300)^{0.5}$	[33, 64]
AR68	$2Ar(^3P_2) \rightarrow 2Ar$	2.00×10^{-13}	[33, 59]
AR69	$Ar(^3P_2) + Ar(^3P_0) \rightarrow 2Ar$	$2.00 \times 10^{-13} \times 2$	[33, 59]
AR70	$2Ar(^3P_0) \rightarrow 2Ar$	2.00×10^{-13}	[33, 59]
AR71	$Ar + Ar^+ \rightarrow Ar + Ar^+$	2.20×10^{-16}	[33, 59]
AR72	$Ar + Ar(4p) \rightarrow Ar + Ar(^3P_2)$	$10^{-16} \times 0.25$	[33, 57]
AR73	$Ar + Ar(4p) \rightarrow Ar + Ar(^3P_1)$	$10^{-16} \times 0.25$	[33, 57]
AR74	$Ar + Ar(4p) \rightarrow Ar + Ar(^3P_0)$	$10^{-16} \times 0.25$	[33, 57]
AR75	$Ar + Ar(4p) \rightarrow Ar + Ar(^1P_1)$	$10^{-16} \times 0.25$	[33, 57]
AR76	$2Ar(^3P_1) \rightarrow e^- + Ar + Ar^+$	5.00×10^{-16} $(T_g/300)^{0.5}$	[33, 64]
AR77	$Ar(^3P_1) + Ar(^1P_1) \rightarrow e^- + Ar + Ar^+$	5.00×10^{-16} $(T_g/300)^{0.5} \times 2$	[33, 64]
AR78	$2Ar(^1P_1) \rightarrow e^- + Ar + Ar^+$	5.00×10^{-16} $(T_g/300)^{0.5}$	[33, 64]
AR79	$2Ar_2^* \rightarrow e^- + 2Ar + Ar_2^+$	5.00×10^{-16}	[33, 57]
AR80	$2Ar + Ar^+ \rightarrow Ar + Ar_2^+$	2.50×10^{-43} $(T_g/300)^{-1.5}$	[33, 64]
AR81	$Ar(^3P_2) + Ar(4p) \rightarrow e^- + Ar + Ar^+$	10^{-15}	[33, 61]
AR82	$Ar(^3P_1) + Ar(4p) \rightarrow e^- + Ar + Ar^+$	10^{-15}	[33, 61]
AR83	$Ar(^3P_0) + Ar(4p) \rightarrow e^- + Ar + Ar^+$	10^{-15}	[33, 61]
AR84	$Ar(^1P_1) + Ar(4p) \rightarrow e^- + Ar + Ar^+$	10^{-15}	[33, 61]
AR85	$2Ar + Ar(4p) \rightarrow Ar + Ar_2^*$	1.10×10^{-44}	[33, 61]
AR86	$2Ar(^3P_2) \rightarrow e + Ar_2^+$	6.30×10^{-16} $(T_g/300)^{-0.5}$	[33, 64]
AR87	$Ar(^3P_2) + Ar(^3P_1) \rightarrow e^- + Ar_2^+$	6.30×10^{-16} $(T_g/300)^{-0.5} \times 2$	[33, 64]
AR88	$Ar(^3P_2) + Ar(^3P_0) \rightarrow e^- + Ar_2^+$	6.30×10^{-16} $(T_g/300)^{-0.5} \times 2$	[33, 64]
AR89	$Ar(^3P_2) + Ar(^1P_1) \rightarrow e^- + Ar_2^+$	6.30×10^{-16} $(T_g/300)^{-0.5} \times 2$	[33, 64]
AR90	$2Ar(^3P_1) \rightarrow e^- + Ar_2^+$	6.30×10^{-16} $(T_g/300)^{-0.5}$	[33, 64]
AR91	$Ar(^3P_1) + Ar(^3P_0) \rightarrow e^- + Ar_2^+$	6.30×10^{-16} $(T_g/300)^{-0.5} \times 2$	[33, 64]
AR92	$Ar(^3P_1) + Ar(^1P_1) \rightarrow e^- + Ar_2^+$	6.30×10^{-16} $(T_g/300)^{-0.5} \times 2$	[33, 64]
AR93	$2Ar(^3P_0) \rightarrow e^- + Ar_2^+$	6.30×10^{-16} $(T_g/300)^{-0.5}$	[33, 64]
AR94	$Ar(^3P_0) + Ar(^1P_1) \rightarrow e^- + Ar_2^+$	6.30×10^{-16} $(T_g/300)^{-0.5} \times 2$	[33, 64]
AR95	$2Ar(^1P_1) \rightarrow e^- + Ar_2^+$	6.30×10^{-16} $(T_g/300)^{-0.5}$	[33, 64]
AR96	$Ar + Ar_2^+ \rightarrow 2Ar + Ar^+$	5.22×10^4 $(11\,608.7/T_g) \times \exp(-1.304 \times 11\,608.7/T_g)$	[33, 65]
AR97	$e^- + Ar_2^+ \rightarrow e^- + Ar + Ar^+$	Cross section, $\sigma(\varepsilon)$	[33, 66]
	SiH_4 and Si_2H_6 reactions		
SR01	$e^- + SiH_4 \rightarrow 2e^- + SiH_3^+ + H$	Cross section, $\sigma(\varepsilon)$	[29, 67, 68]
SR02	$e^- + SiH_4 \rightarrow 2e^- + SiH_2^+ + H_2$	Cross section, $\sigma(\varepsilon)$	[29, 67, 68]
SR03	$e^- + SiH_4 \rightarrow 2e^- + SiH^+ + H_2 + H$	Cross section, $\sigma(\varepsilon)$	[29, 67, 68]
SR04	$e^- + SiH_4 \rightarrow 2e^- + Si^+ + H_2 + H_2$	Cross section, $\sigma(\varepsilon)$	[29, 67, 68]
SR05	$e^- + SiH_4 \rightarrow e^- + SiH_3 + H$	Cross section, $\sigma(\varepsilon)$	[29, 67, 69]
SR06	$e^- + SiH_4 \rightarrow e^- + SiH_2 + 2H$	Cross section, $\sigma(\varepsilon)$	[29, 67, 69]
SR07	$e^- + SiH_4 \rightarrow e^- + SiH_4^{(1-3)}$	Cross section, $\sigma(\varepsilon)$	[29, 67, 70]
SR08	$e^- + SiH_4 \rightarrow e^- + SiH_4^{(2-4)}$	Cross section, $\sigma(\varepsilon)$	[29, 67, 70]
SR09	$e^- + SiH_4 \rightarrow SiH_3^- + H$	Cross section, $\sigma(\varepsilon)$	[29, 67, 71]
SR10	$e^- + SiH_4 \rightarrow SiH_2^- + H_2$	Cross section, $\sigma(\varepsilon)$	[29, 67, 71]
SR11	$e^- + Si_2H_6 \rightarrow 2e^- + Si_2H_4^+ + 2H$	Cross section, $\sigma(\varepsilon)$	[29, 67, 68]
SR12	$e^- + Si_2H_6 \rightarrow e^- + SiH_3 + SiH_2 + H$	Cross section, $\sigma(\varepsilon)$	[29, 67, 69]

(Continued.)

Table A1. (Continued.)

SR13	$e^- + SiH_3^+ \rightarrow SiH_2 + H$	$1.69 \times 10^{-13}\ T_e^{-0.5}$	[29, 67]
SR14	$e^- + SiH_2^+ \rightarrow SiH + H$	$1.69 \times 10^{-13}\ T_e^{-0.5}$	[29, 67]
	H_2 reactions		
HR01	$e^- + H_2 \rightarrow 2e^- + H_2^+$	Cross section, $\sigma(\varepsilon)$	[67, 72–74]
HR02	$e^- + H_2 \rightarrow 2e^- + H^+ + H$	Cross section, $\sigma(\varepsilon)$	[67, 72–74]
HR03	$e^- + H_2 \rightarrow e^- + 2H$	Cross section, $\sigma(\varepsilon)$	[67, 72–74]
HR04	$e^- + H_2 \rightarrow e^- + H_2^{(v=1)}$	Cross section, $\sigma(\varepsilon)$	[67, 72–74]
HR05	$e^- + H_2 \rightarrow e^- + H_2^{(v=2)}$	Cross section, $\sigma(\varepsilon)$	[67, 72–74]
HR06	$e^- + H_2 \rightarrow e^- + H_2^{(v=3)}$	Cross section, $\sigma(\varepsilon)$	[67, 72–74]
HR07	$e^- + H_3^+ \rightarrow H_2 + H$	$9.75 \times 10^{-14}\ T_e^{-0.5}$	[67, 75]
HR08	$e^- + H_2^+ \rightarrow H + H$	$5.66 \times 10^{-14}\ T_e^{-0.5}$	[67, 75]
HR09	$e^- + H^+ \rightarrow H + h\nu$	$2.62 \times 10^{-19}\ T_e^{-0.5}$	[67, 75]

ORCID iD

Ho Jun Kim https://orcid.org/0000-0002-6752-8905

References

[1] Arts K, Hamaguchi S, Ito T, Karahashi K, Knoops H C M, Mackus A J M and Kessels W M M E 2022 Foundations of atomic-level plasma processing in nanoelectronics *Plasma Sources Sci. Technol.* **31** 103002

[2] Hori M 2022 Radical-controlled plasma processes *Rev. Mod. Plasma Phys.* **6** 36

[3] Snyders R, Hegemann D, Thiry D, Zabeida O, Klemberg-Sapieha J and Martinu L 2023 Foundations of plasma enhanced chemical vapor deposition of functional coatings *Plasma Sources Sci. Technol.* **32** 074001

[4] Knoops H C M, Faraz T, Arts K and Kessels W M M E 2019 Status and prospects of plasma-assisted atomic layer deposition *J. Vac. Sci. Technol.* A **37** 030902

[5] Maydan D 2001 The future of equipment development and semiconductor production *Mater. Sci. Eng.* A **302** 1–5

[6] Hwang S and Kanarik K (available at: https://sst.semiconductor-digest.com/2016/08/evolution-of-across-wafer-uniformity-control-in-plasma-etch/)

[7] Abdel-Fattah E and Sugai H 2013 Combined effects of gas pressure and exciting frequency on electron energy distribution functions in hydrogen capacitively coupled plasmas *Phys. Plasmas* **20** 023501

[8] Kim H J 2021 Influence of the gas pressure in a Torr regime capacitively coupled plasma deposition reactor *Plasma Sources Sci. Technol.* **30** 065001

[9] Bera K, Rauf S, Ramaswamy K and Collins K 2009 Effects of interelectrode gap on high frequency and very high frequency capacitively coupled plasmas *J. Vac. Sci. Technol.* A **27** 706

[10] Agarwal A, Rauf S and Collins K 2012 Gas heating mechanisms in capacitively coupled plasmas *Plasma Sources Sci. Technol.* **21** 055012

[11] Hegemann D, Michlíček M, Blanchard N E, Schütz U, Lohmann D, Vandenbossche M, Zajíčková L and Drábik M 2016 Deposition of functional plasma polymers influenced by reactor geometry in capacitively coupled discharges *Plasma Process. Polym.* **13** 279

[12] Donkó Z, Hartmann P, Korolov I, Schulenberg D, Rohr S, Rauf S and Schulze J 2023 Metastable argon atom kinetics in a low-pressure capacitively coupled radio frequency discharge *Plasma Sources Sci. Technol.* **32** 065002

[13] Moravej M, Yang X, Nowling G R, Chang J P, Hicks R F and Babayan S E 2004 Physics of high-pressure helium and argon radio-frequency plasmas *J. Appl. Phys.* **96** 7011–7

[14] Hofmann S, Gessel A F H V, Verreycken T and Bruggeman P 2011 Power dissipation, gas temperatures and electron densities of cold atmospheric pressure helium and argon RF plasma jets *Plasma Sources Sci. Technol.* **20** 065010

[15] Wang W, Rong M, Murphy A B, Wu Y, Spencer J W, Yan J D and Fang M T C 2011 Thermophysical properties of carbon–argon and carbon–helium plasmas *J. Phys. D: Appl. Phys.* **44** 355207

[16] Shao X J, Jiang N, Zhang G J and Cao Z X 2012 Comparative study on the atmospheric pressure plasma jets of helium and argon *Appl. Phys. Lett.* **101** 253509

[17] Takamatsu T, Uehara K, Sasaki Y, Miyahara H, Matsumura Y, Iwasawa A, Ito N, Azuma T, Kohno M and Okino A 2014 Investigation of reactive species using various gas plasmas *RSC Adv.* **4** 39901

[18] Gul B and Aman-ur-Rehman 2015 A comparative study of capacitively coupled HBr/He, HBr/Ar plasmas for etching applications: numerical investigation by fluid model *Phys. Plasmas* **22** 103520

[19] Golda J, Held J and Gathen V S V D 2020 Comparison of electron heating and energy loss mechanisms in an RF plasma jet operated in argon and helium *Plasma Sources Sci. Technol.* **29** 025014

[20] Zhang B and Zhang X 2020 Control of higher-silane generation by dilution gases in SiH_4 plasmas *Plasma Sources Sci. Technol.* **29** 095012

[21] Kim H J and Lee H J 2017 Analysis of intermediate pressure SiH_4/He capacitively coupled plasma for deposition of an amorphous hydrogenated silicon film in consideration of thermal diffusion effects *Plasma Sources Sci. Technol.* **26** 085003

[22] Kim H J 2021 Effect of electrode heating on the distribution of the ion production rate in a capacitively coupled plasma deposition reactor in consideration of thermal decomposition *Vacuum* **189** 110264

[23] Bhandarkar U, Kortshagen U and Girshick S L 2003 Numerical study of the effect of gas temperature on the time for onset of particle nucleation in argon–silane low-pressure plasmas *J. Phys. D: Appl. Phys.* **36** 1399–408

[24] Gordiets B F, Inestrosa-Izurieta M J, Navarro A and Bertran E 2011 Nanoparticles in SiH_4-Ar plasma: modelling and comparison with experimental data *J. Appl. Phys.* **110** 103302

[25] Santos B, Cacot L, Boucher C and Vidal F 2019 Electrostatic enhancement factor for the coagulation of silicon nanoparticles in low-temperature plasmas *Plasma Sources Sci. Technol.* **28** 045002

[26] Lanham S J, Polito J, Shi X, Elvati P, Violi A and Kushner M J 2021 Scaling of silicon nanoparticle growth in low temperature flowing plasmas *J. Appl. Phys.* **130** 163302

[27] Tamadate T and Hogan C J Jr 2022 Silicon nanocluster anion-argon cation recombination via hybrid continuum-molecular dynamics calculations *J. Aerosol Sci.* **163** 105994

[28] Kushner M J 1988 A model for the discharge kinetics and plasma chemistry during plasma enhanced chemical vapor deposition of amorphous silicon *J. Appl. Phys.* **63** 2532–51

[29] Perrin J, Leroy O and Bordage M C 1996 Cross-sections, rate constants and transport coefficients in silane plasma chemistry *Contrib. Plasma Phys.* **36** 3–49

[30] Perrin J, Shiratani M, Kae-Nune P, Videlot H, Jolly J and Guillon J 1998 Surface reaction probabilities and kinetics of H, SiH_3, Si_2H_5, CH_3, and C_2H_5 during deposition of a-Si:H and a-C:H from H_2, SiH_4, and CH_4 discharges *J. Vac. Sci. Technol.* A **16** 278

[31] Park H, Yoon E, Lee G-D and Kim H J 2019 Analysis of surface adsorption kinetics of SiH_4 and Si_2H_6 for deposition of a hydrogenated silicon thin film using intermediate pressure SiH_4 plasmas *Appl. Surf. Sci.* **496** 143728

[32] Park H and Kim H J 2021 Theoretical analysis of Si_2H_6 adsorption on hydrogenated silicon surfaces for fast deposition using intermediate pressure SiH_4 capacitively coupled plasma *Coatings* **11** 1041

[33] Cheon C, Yoon J H, Jo S, Kim H J and Lee H J 2022 Importance of higher-level excited species in argon remote plasma sources: numericalmodeling with consideration of detailed chemical reaction pathways *Plasma Process. Polym.* **19** 2100251

[34] Coltrin M E, Kee R J and Miller J A 1984 A mathematical model of the coupled fluid mechanics and chemical kinetics in a chemical vapor deposition reactor *J. Electrochem. Soc.* **131** 425

[35] Piper L G, Velazco J E and Setser D W 1973 Quenching cross sections for electronic energy transfer reactions between metastable argon atoms and noble gases and small molecules *J. Chem. Phys.* **59** 3323–40

[36] Theard L P, Wesley J and Huntress T 1974 Ion-molecule reactions and vibrational deactivation of H_2^+ ions in mixtures of hydrogen and helium *J. Chem. Phys.* **60** 2840–8

[37] Allen W N, Cheng T M H and Lampe F W 1977 Ion–molecule reactions in SiH_4–D_2 mixtures *J. Chem. Phys.* **66** 3371–5

[38] Chatham H and Gallagher A 1985 Ion chemistry in silane dc discharges *J. Appl. Phys.* **58** 159–69

[39] Henis J M S, Stewart G W, Tripodi M K and Gaspar P P 1972 Ion-molecule reactions in silane *J. Chem. Phys.* **57** 389–98

[40] Henis J M S, Stewart G W and Gaspar P P 1973 Endothermic ion-molecule reactions in silane *J. Chem. Phys.* **58** 3639–46

[41] Cheng T M H, Yu T Y and Lampe F W 1974 Ion-molecule reactions in disilane *J. Phys. Chem.* **78** 1184–9

[42] Austin E R and Lampe F W 1977 Rate constants for the reactions of hydrogen atoms with some silanes and germanes *J. Phys. Chem.* **81** 1134

[43] Jasinski J M and Chu J O 1988 Absolute rate constants for the reaction of silylene with hydrogen, silane, and disilane *J. Chem. Phys.* **88** 1678–87

[44] Coltrin M E, Kee R J and Miller J A 1986 A mathematical model of silicon chemical vapor deposition: further refinements and the effects of thermal diffusion *J. Electrochem. Soc.* **133** 1206

[45] Itabashi N, Nishiwaki N, Magane M, Naito S, Goto T, Matsuda A, Yamada C and Hirota E 1990 Spatial distribution of SiH_3 radicals in RF silane plasma *Jpn. J. Appl. Phys.* **29** L505

[46] Moore C B 1965 Vibration-rotation energy transfer *J. Chem. Phys.* **43** 2979–86

[47] Kim J H *et al* 2019 Advanced measurement and diagnosis of the effect on the underlayer roughness for industrial standard metrology *Sci. Rep.* **9** 1018

[48] Kushner M J 1992 Simulation of the gas-phase processes in remote-plasma-activated chemical-vapor deposition of silicon dielectrics using rare gas-silane-ammonia mixtures *J. Appl. Phys.* **9** 4173–89

[49] Chatham H, Hils D, Robertson R and Gallagher A C 1983 Reactions of He^+, Ne^+, and Ar^+ with CH_4, C_2H_6, SiH_4, and Si_2H_6 *J. Chem. Phys.* **79** 1301–11

[50] Schulze J, Derzsi A, Dittmann K, Hemke T, Meichsner J and Donkó Z 2011 Ionization by drift and ambipolar electric fields in electronegative capacitive radio frequency plasmas *Phys. Rev. Lett.* **107** 275001

[51] Lieberman M A and Lichtenberg A J 2005 *Principles of Plasma Discharges and Materials Processing* (Wiley)

[52] Vahedi V 1993 *Modeling and Simulation of RF Discharges Used for Plasma Processing* (University of California)

[53] Gudmundsson J T 2002 Notes on the electron excitation rate coefficients for argon and oxygen discharge Report RH-21-2002 (University of Iceland)

[54] Tachibana K 1986 Excitation of the $1s_5$, $1s_4$, $1s_3$, and $1s_2$ levels of argon by low-energy electrons *Phys. Rev.* A **34** 1007–15

[55] Eggarter E 1975 Comprehensive optical and collision data for radiation action. II. Ar *J. Chem. Phys.* **62** 833–47

[56] Ashida S, Lee C and Lieberman M A 1995 Spatially averaged (global) model of time modulated high density argon plasmas *J. Vac. Sci. Technol.* A **13** 2498–507

[57] Kannari F, Obara M and Fujioka T 1985 An advanced kinetic model of electron-beam-excited KrF lasers including the vibrational relaxation in KrF^*(B) and collisional mixing of KrF^*(B,C) *J. Appl. Phys.* **57** 4309–22

[58] Bogaerts A 2009 Hybrid Monte Carlo—fluid model for studying the effects of nitrogen addition to argon glow discharges *Spectrochim. Acta* B **64** 126–40

[59] Gudmundsson J T and Thorsteinsson E G 2007 Oxygen discharges diluted with argon: dissociation processes *Plasma Sources Sci. Technol.* **16** 399

[60] Vriens L and Smeets A H M 1980 Cross-section and rate formulas for electron-impact ionization, excitation, deexcitation, and total depopulation of excited atoms *Phys. Rev.* A **22** 940–51

[61] Arakoni R A, Bhoj A N and Kushner M J 2007 H_2 generation in Ar/NH_3 microdischarges *J. Phys. D: Appl. Phys.* **40** 2476–90

[62] Bogaerts A and Gijbels R 1995 Modeling of metastable argon atoms in a direct-current glow discharge *Phys. Rev.* A **52** 3743

[63] Lee Y-K and Chung C-W 2011 Ionization in inductively coupled argon plasmas studied by optical emission spectroscopy *J. Appl. Phys.* **109** 013306

[64] Kang N, Gaboriau F, Oh S-G and Ricard A 2011 Modeling and experimental study of molecular nitrogen dissociation in an Ar–N_2 ICP discharge *Plasma Sources Sci. Technol.* **20** 045015

[65] Henriques J, Tatarova E and Ferreira C M 2011 Microwave N_2-Ar plasma torch. I. Modeling *J. Appl. Phys.* **109** 023301

[66] Treshchalov A B and Lissovski A A 2009 VUV-VIS spectroscopic diagnostics of a pulsed high-pressure discharge in argon *J. Phys. D: Appl. Phys.* **42** 245203

[67] Kim H J, Yang W and Joo J 2015 Effect of electrode spacing on the density distributions of electrons, ions, and metastable and radical molecules in SiH_4/NH_3/N_2/He capacitively coupled plasmas *J. Appl. Phys.* **118** 043304

[68] Krishnakumar E and Srivastava S K 1995 Ionization cross sections of silane and disilane by electron impact *Contrib. Plasma Phys.* **35** 395–404

[69] Perrin J, Schmitt J P M, de Rosny G, Drevillon B, Huc J and Lloret A 1982 Dissociation cross sections of silane and disilane by electron impact *Chem. Phys.* **73** 383–94
[70] Kurachi M and Nakamura Y 1989 Electron collision cross sections for the monosilane molecule *J. Phys. D: Appl. Phys.* **22** 107–12
[71] Haaland P 1990 Dissociative attachment in silane *J. Chem. Phys.* **93** 4066–72
[72] Phelps A V (available at: ftp://jila.colorado.edu/collision_data)
[73] Phelps A V 1990 Cross sections and swarm coefficients for H^+, H_2^+, H_3^+, H, H_2 and H^- in H_2 for energies from 0.1 eV to 10 keV *J. Phys. Chem. Ref. Data* **19** 653–75
[74] Tawara H, Itikawa Y, Nishimura H and Yoshino M 1990 Cross sections and related data for electron collisions with hydrogen molecules and molecular ions *J. Phys. Chem. Ref. Data* **19** 617–36
[75] Salabas A 2003 Fluid model for charged particle transport in capacitively coupled radio-frequency discharges (Instituto Superior Tecnico, Universidade Técnica de Lisboa)